

# Prediction of the Effect of Heat Treatment on the Susceptibility of Fe-Ni-Cr-Mo Alloys to Localized Corrosion

Andre Anderko<sup>1\*</sup>, Narasi Sridhar<sup>2</sup>, and Garth Tormoen<sup>3</sup>

<sup>1</sup> OLI Systems Inc, 108 American Road, Morris Plains, NJ 07950

<sup>2</sup> Det Norske Veritas, 5777 Frantz Road, Dublin, OH 43017

<sup>3</sup> Southwest Research Institute, Department of Materials Engineering, 6220 Culebra Road, San Antonio, TX 78238

\* Corresponding author, e-mail: aanderko@olisystems.com

## Abstract

A model has been developed for evaluating the effect of thermal aging on the repassivation potential of austenitic alloys. The model consists of two parts – a grain boundary microchemistry model for calculating the chromium and molybdenum depletion profiles in the vicinity of grain boundaries and an electrochemical model that relates the repassivation potential to the microchemistry and environmental conditions including temperature and solution chemistry. The grain boundary microchemistry model incorporates a thermodynamic para-equilibrium treatment of the formation of carbides and a kinetic treatment of the diffusion of Cr and Mo. With this model, experimental Cr and Mo depletion profiles can be reproduced for sensitized alloys 600, 825, and 316L. The repassivation potential model accounts for the effects of solution chemistry and temperature by considering competitive dissolution, adsorption and oxide formation processes at the interface between the metal and the occluded site solution. Using a previously established relationship between the repassivation potential and alloy composition, a procedure has been established to calculate the observable repassivation potential by integrating its local values that reflect the alloy microchemistry in the depletion zone. The predicted repassivation potentials agree with experimental data for thermally aged alloys 600 and 825 in chloride solutions.

**Keywords:** Localized corrosion, alloys 600, 825, and 22, repassivation potential, thermal aging

## Introduction

Localized corrosion of engineering alloys is a complex function of metallurgical factors and environmental conditions. Among metallurgical factors, effects of thermal instabilities are of interest for assessing the performance and expected service life of industrial components fabricated from nominally corrosion-resistant stainless steels and nickel-base alloys. Fabrication processes such as heat treatment and welding are known to introduce microstructural changes that may affect both the structural and corrosion performance of an alloy. In particular, thermal instability of stainless steels and nickel-base alloys may lead to the formation of complex metal carbides of the type  $M_3C_2$ ,  $M_7C_3$ ,  $M_6C$ , or  $M_{23}C_6$  in which the metallic component M represents Cr, Mo, W, and Fe. The carbide is chromium- or molybdenum-rich depending on the carbide type, which in turn depends on the alloy composition and temperature. Also, chromium-rich intermetallic phases such as the  $\sigma$ ,  $\chi$ , R, and  $\mu$  phases can form in many alloys.<sup>1,2</sup> Precipitation of such phases may occur at temperatures ranging from 500 to 900 °C depending on alloy composition. Formation of grain boundary carbides often results in the depletion of chromium and, possibly, molybdenum in the vicinity of the grain boundary because of the slow diffusion of substitutional elements such as chromium relative to the interstitial carbon. Similarly, the corrosion resistance of welded components may be affected by the segregation of alloying elements and precipitation of intermetallic phases, carbides or nitrides in the solidified weld and unmixed zones as well as the precipitation of carbides and other phases in the heat-affected zone adjacent to the weld.<sup>3</sup>

Sensitization of Fe-Ni-Cr-Mo alloys and its effects on intergranular attack and intergranular stress corrosion cracking has been extensively modeled in the literature.<sup>4-13</sup> Much less effort has been devoted to pitting and crevice corrosion of thermally aged and fabricated alloys. Most of the studies of localized corrosion of thermally aged or welded stainless steels and Ni-base alloys have been focused on developing comparative performance data in specific environments, for example critical crevice temperatures in ferric chloride solutions. Recent localized corrosion studies have been focused on characterizing the dependence of localized corrosion parameters in certain environments on thermal aging of Ni-base alloys, i.e., alloy 825<sup>14</sup> and alloy 22.<sup>15-17</sup> In the first part of this study,<sup>18</sup> the localized corrosion of alloy 600 was investigated. However, no generalized treatment has been proposed so far to rationalize and predict the effects of heat treatment on the susceptibility of Fe-Ni-Cr-Mo alloys to pitting or crevice corrosion.

In previous papers,<sup>19,20</sup> a computational methodology was proposed to predict the tendency of base metals to undergo localized corrosion. This methodology is based on the computation of two characteristic parameters as functions of aqueous environment composition and temperature, i.e., the corrosion potential ( $E_{\text{corr}}$ ) and the repassivation potential ( $E_{\text{rp}}$ ), also called the protection potential. The repassivation potential provides a threshold condition below which stable pitting or crevice corrosion does not occur.<sup>19,21,22</sup>  $E_{\text{rp}}$  is amenable to modeling because it is relatively insensitive to surface finish and coincides for pitting and crevice corrosion as long as propagation exceeds a certain minimum value.<sup>22</sup> The values of  $E_{\text{rp}}$  and  $E_{\text{corr}}$ , calculated as a function of environmental conditions, can be then compared to determine the susceptibility of an alloy to localized corrosion.<sup>20,22</sup> To predict the repassivation potential as a function of environmental conditions, a mechanistic model was developed in a previous paper.<sup>19</sup> This model was shown to reproduce  $E_{\text{rp}}$  for a number of alloys in laboratory solutions and in complex

chemical process environments.<sup>23</sup> The repassivation potential model can be used as a predictive tool for alloys in multicomponent industrial environments because its parameters are expressed as functions of aqueous solution chemistry. Moreover, the  $E_{rp}$  model parameters have been correlated with the composition of Fe-Ni-Cr-Mo-W-N alloys,<sup>24</sup> thus making it possible to predict the effect of compositional variations in an alloy on  $E_{rp}$ .

The objective of this study is to find a quantitative relationship between the repassivation potential and the microstructural changes that are associated with thermal instabilities. For this purpose, a new model was developed for predicting the chromium and molybdenum depletion profiles that occur at grain boundaries as a result of sensitization. Then, the new grain boundary chemistry model was combined with the previously developed repassivation potential model to predict  $E_{rp}$  of thermally aged alloys or alloys with compositional changes due to element segregation during solidification. This allows a link to be established between the microstructural variations in alloy composition and the observable, macroscopic values of the repassivation potential, thus providing a threshold condition for localized corrosion. Further, the predictions are verified using previously obtained repassivation potential data for thermally aged alloys 600 and 825 and welded alloy 22.

## **Experimental Database**

The modeling studies reported here rely on the previous experimental results of Tormoen et al.<sup>18</sup> and Pan et al.<sup>14</sup> for the repassivation potential of heat-treated alloys 600 and 825, respectively. Additionally, the repassivation potential data reported by Dunn et al.<sup>15-17</sup> were used for welded samples of alloy 22. The nominal compositions of the alloys studied here are summarized in Table 1. In addition to the repassivation potential data, depletion profile data for alloys 600, 825, and 316L are used to verify the grain boundary composition model.

## **Computational Model**

The computational model developed in this study consists of three parts, i.e.

- (1) A grain boundary microchemistry model for predicting the chromium and molybdenum depletion in the vicinity of grain boundaries as a result of carbide formation;
- (2) An electrochemical model for calculating the repassivation potential of Fe-Ni-Cr-Mo-W alloys as a function of alloy composition and environmental conditions including temperature and concentrations of aqueous solution species;
- (3) A procedure for calculating the observable repassivation potential that corresponds to macroscopic localized corrosion by applying the electrochemical model to the depletion profiles and performing suitable integration.

### ***Grain boundary microchemistry model***

In the last four decades, several computational models have been developed to predict the redistribution of alloying elements in the vicinity of grain boundaries.<sup>4,10,11,13,25-27,28-31</sup> The motivation for these studies was to be able to understand and quantitatively predict intergranular attack (IGA) and intergranular stress corrosion cracking (IGSCC), which are controlled by the

depletion of chromium in a region adjacent to the grain boundary. The models developed in the literature can be roughly divided into two classes, i.e.,

- (i) Models that combine a thermodynamic equilibrium formalism for metal carbide formation with a kinetic treatment of the redistribution of Cr and other elements as a function of the distance from the grain boundary<sup>4,10,11,25,26,28,30</sup> and
- (ii) Models that rely on a kinetic treatment of the evolution of grain boundary chromium concentration without explicitly invoking thermodynamic relationships for the local equilibrium associated with carbide formation.<sup>13,29,31</sup> Such an approach can be used to facilitate separating the stages of chromium depletion and self-healing<sup>29</sup> or to introduce a detailed, three-dimensional treatment of the growth kinetics of carbides.<sup>31</sup>

The literature models have been successful in predicting the Cr depletion profiles<sup>10,11,13,29</sup> and the critical conditions of sensitization as investigated using electrochemical potentiokinetic reactivation<sup>28</sup> and IGA/IGCC susceptibility data.<sup>11,13</sup> Much less attention has been devoted to molybdenum depletion, primarily because Mo depletion data are much less abundant in the literature. However, the computation of Mo depletion profiles is of great interest here because of the importance of Mo in localized corrosion.

In this study, we develop a grain boundary microchemistry model that serves as a foundation for predicting the effect of heat treatment on localized corrosion. While we utilize the concepts introduced in the combined thermodynamic/kinetic models mentioned above, we construct the model in a way that is particularly suitable for applications to localized corrosion prediction. For this purpose, the model is designed to satisfy the following requirements:

- (1) It should be applicable to the prediction of Mo depletion as well as Cr depletion as a function of temperature and time of heat exposure.
- (2) It should make it possible to predict the effects of variations in bulk alloy composition and, in particular, the alloy's carbon content rather than merely fit the depletion profiles for individual alloys. This requirement necessitates the use of a thermodynamic model for the alloy phase.
- (3) The model parameters should be limited to quantities that have a well-defined physical meaning, can be obtained from independent experimental data or can be reasonably estimated and are readily transferable to similar alloys. This requirement effectively limits the model to the use of thermodynamic functions of formation of carbides, thermodynamic parameters for activity coefficients in solid solutions, diffusion coefficients and simple structural parameters such as the average grain size.
- (4) The computations should be reasonably fast because they need to be performed numerous times. This means that we endeavor to develop analytical expressions, whenever possible, rather than numerically solving the pertinent diffusion equations. Therefore, multicomponent diffusion effects<sup>30</sup> are not taken into account and diffusion equations are written in terms of concentrations of individual alloy components.

To develop a simple model for calculating the depletion profiles as a function of temperature and time of heat exposure and bulk alloy composition, we adopt the following assumptions:

- (a) The precipitating carbides can be treated as if they form a grain boundary film of equivalent, averaged thickness and, consequently, the diffusion in the matrix can be treated as one-dimensional. Grain boundary diffusion can be assumed to be sufficiently rapid to establish equilibrium along the grain boundaries between carbide particles and the adjacent region of the matrix. In reality, grain boundary precipitates are often discontinuous, a fact that is used in measuring grain boundary depletion profiles without interference from the carbides. However, for model simplification, we assume that these discontinuous particles can be treated as if they coat the grain boundaries uniformly.
- (b) Since the interstitial diffusion of carbon is several orders of magnitude faster than the diffusion of substitutional elements (i.e., Cr, Mo, Ni, and Fe), carbon activity can be assumed to be equal throughout the material.
- (c) At the carbide-matrix interface, local thermodynamic equilibrium (or para-equilibrium) is assumed. This equilibrium is determined by the local activity of Cr and Mo and the global activity of C.
- (d) At a sufficiently long distance from the grain boundary, the concentrations of substitutional elements are the same as those in the bulk alloy because the amount of these elements precipitated as carbides is negligibly small compared to their original amounts. On the other hand, the concentration of carbon decreases appreciably as the process of carbide formation advances.
- (e) The carbides may be of the form  $M_7C_3$  or  $M_{23}C_6$  and contain only Cr and, if applicable, Mo in addition to carbon. While we do not consider other carbide phase compositions in this study, an extension of the model to other stoichiometries would be straightforward.
- (f) Carbide nucleation and incubation time are neglected and the model deals only with the growth of the carbides.
- (g) Carbide growth is controlled by the diffusion of the metallic component of the carbide. The diffusion coefficients are independent of concentration.
- (h) The moving boundary at the carbide-matrix is ignored in diffusion calculations. This implies that the thickness of the carbide is negligible in comparison to the grain diameter.

For simplicity, the computation of chromium depletion profiles is described first and then its extension to treat molybdenum depletion is presented.

### *Calculation of Cr depletion*

The variables used in the microchemistry model are defined in Figure 1. It is assumed that the concentrations of Cr in the bulk alloy and in the carbide phase ( $\beta$ ) are  $C_{Cr}^0$  and  $C_{Cr}^\beta$ , respectively. The concentration of Cr at the matrix ( $\gamma$ ) - carbide ( $\beta$ ) interface is given by  $C_{Cr}^{\gamma\beta}$  and results from the para-equilibrium between the carbide phase and Cr and C from the matrix. At a given instant of time  $t$ , the carbide thickness is  $r$  and the concentration of Cr in the matrix is a function of the distance from the grain boundary,  $z$ , and is given by the function  $C_{Cr}^\gamma(z)$ . The area of the rectangle C represents the accumulation of Cr in the carbide at a given instant of time. The consumption of chromium as a result of carbide growth is balanced by the diffusion of Cr from the bulk, which results in a Cr concentration gradient as given by  $C_{Cr}^\gamma(z)$ . Thus, the area C is always equal to the chromium content that has been withdrawn from the depleted zone,  $D$ .<sup>4,13</sup> The mass balance for chromium (Fig. 1, upper diagram) is inextricably linked with the mass

balance for carbon (Fig. 1, lower diagram). Simultaneously with the accumulation of Cr within the carbide, carbon is progressively consumed and its concentration drops throughout the grain. While the activity of carbon remains constant within the grain, its concentration develops a certain profile in the vicinity of the grain boundary as a function of  $z$  (cf.  $C_C^\gamma(z)$  in Fig. 1, lower diagram) because the activity coefficient of carbon varies with the changing concentration of Cr and other elements. The drop in the matrix concentration of carbon (i.e., from the original concentration of  $C_C^0$  to  $C_C^\gamma$ ) entails a drop in the interface concentration to  $C_C^{\gamma\beta}$  until the matrix carbon concentration reaches the solubility limit. The interface concentrations of carbon,  $C_C^{\gamma\beta}$ , and chromium,  $C_{Cr}^{\gamma\beta}$ , are linked through the thermodynamic equilibrium of carbide formation:

$$\nu_{Cr}Cr + \nu_C C = Cr_{\nu_{Cr}} C_{\nu_C} \quad (1)$$

where  $\nu_{Cr}$  and  $\nu_C$  are the stoichiometric coefficients of chromium and carbon within the carbide, respectively.

Thus, the growth of the carbide and the corresponding evolution of the concentration profiles is controlled by the flow of carbon as well as chromium to the interface. Since the available amount of carbon is finite within a grain, the depletion profile will depend on the grain size, which determines the available volume from which carbon can be withdrawn to form the carbide. The conservation of mass requires that the areas Y and Z in Fig. 1 (lower diagram) be equal to each other because the carbon content in the carbide (Y) is equal to the amount of carbon withdrawn from the matrix (Z). The model must simultaneously satisfy the two mass balance conditions, i.e.,  $C = D$  and  $Y = Z$ .

Since the model is assumed to be one-dimensional, the chromium concentration profile can be obtained from Fick's second law, i.e.,

$$\frac{\partial C_{Cr}}{\partial t} = D_{Cr} \frac{\partial^2 C_{Cr}}{\partial z^2} \quad (2)$$

where  $D_{Cr}$  is the diffusion coefficient of Cr. The concentration profile can be expressed as a function of time,  $t$ , and distance from the grain boundary,  $z$ , using the error function solution,<sup>32,13</sup>

$$C_{Cr}^\gamma(z, t) = C_{Cr}^{\gamma\beta} + (C_{Cr}^0 - C_{Cr}^{\gamma\beta}) \operatorname{erf} \left( \frac{z}{2\sqrt{D_{Cr}t}} \right) \quad (3)$$

where the superscripts denote the phases and have been explained in Figure 1. Since the concentration of component  $i$ ,  $C_i$ , is related to its mole fraction  $x_i$  and molar volume of the matrix  $V_m$  by

$$C_i = \frac{x_i}{V_m} \quad (i = \text{Cr, Fe, Ni, C, } \dots) \quad (4)$$

eq. (2) can be rewritten in a more convenient form using mole fractions, i.e.,

$$x_{Cr}^\gamma(z, t) = x_{Cr}^{\gamma\beta} + (x_{Cr}^0 - x_{Cr}^{\gamma\beta}) \operatorname{erf}\left(\frac{z}{2\sqrt{D_{Cr}t}}\right) \quad (5)$$

The accumulation of Cr in the carbide phase, as depicted by area C in Figure 1, is given by

$$\Delta n_{Cr}^\beta = (C_{Cr}^\beta - C_{Cr}^0) S \bar{r} \quad (6)$$

where  $S$  is the surface area of the grain and  $\bar{r}$  is the average thickness of the carbide phase along the  $z$  axis. The total depletion of Cr in the grain can be calculated by integrating the local depletion over the entire grain, i.e.,

$$\Delta n_{Cr}^\gamma = \int_0^\infty (C_{Cr}^0 - C_{Cr}^\gamma(z, t)) dz \quad (7)$$

In eq. (7), the integral is calculated from 0 to infinity even though the size of the grain is finite. However, this is justified by the fact that the dimension of the depletion zone is much smaller than the size of the grain as the local concentration of Cr rapidly approaches the original concentration ( $C_{Cr}^0$ ) at a sufficiently large distance from the depletion zone. By substituting eqs. (4) and (5) into eq. (7), we obtain:

$$\Delta n_{Cr}^\gamma = \frac{S(x_{Cr}^0 - x_{Cr}^{\gamma\beta})}{V_m^\gamma} \int_0^\infty \operatorname{erfc}\left(\frac{z}{2\sqrt{D_{Cr}t}}\right) dz \quad (8)$$

Considering that the definite integral of the complementary error function  $\operatorname{erfc}$  is

$$\int_0^\infty \operatorname{erfc}(q) dq = \frac{1}{\sqrt{\pi}} \quad (9)$$

eq. (8) becomes:

$$\Delta n_{Cr}^\gamma = \frac{S(x_{Cr}^0 - x_{Cr}^{\gamma\beta}) 2\sqrt{D_{Cr}t}}{V_m^\gamma \sqrt{\pi}} \quad (10)$$

The mass balance of Cr requires that

$$\Delta n_{Cr}^{\beta} = \Delta n_{Cr}^{\gamma} \quad (11)$$

By substituting eqs. (6) and (10) into eq. (11) and utilizing eq. (4), we obtain a condition for the quantity  $\bar{r}$ :

$$\bar{r} = \frac{V_m^{\beta} (x_{Cr}^0 - x_{Cr}^{\gamma\beta}) 2\sqrt{D_{Cr}t}}{V_m^{\gamma} (x_{Cr}^{\beta} - x_{Cr}^0) \sqrt{\pi}} \quad (12)$$

The accumulation of carbon in the carbide phase is given by an equation analogous to eq. (6):

$$\Delta n_C^{\beta} = (C_C^{\beta} - C_C^0) S \bar{r} \quad (13)$$

where  $C_C^{\beta}$  and  $C_C^0$  are the concentrations of carbon in the carbide phase and in the original alloy, respectively (cf. Fig.1, lower diagram). The quantity  $C_C^{\beta}$  (and, hence,  $x_C^{\beta}$ ) results directly from the assumed stoichiometry of the carbide. The total depletion of C in the grain can be calculated as

$$\Delta n_C^{\gamma} = (C_C^0 - \bar{C}_C^{\gamma}) S d \quad (14)$$

where  $\bar{C}_C^{\gamma}$  is the average concentration of carbon in the grain and  $d$  is the average distance from which carbon can be withdrawn. In eq. (14), the average concentration  $\bar{C}_C^{\gamma}$  is used instead of integrating the carbon concentration,  $C_C^{\gamma}$ , throughout the grain. This approximation introduces a negligible error because the activity of carbon shows a certain gradient only in the vicinity of the grain boundary (cf. Fig. 1), due to the change in the activity coefficient of carbon with the change in the concentration of substitutional elements. However, the size of the depletion zone is substantially smaller than the size of the grain. Hence, the distance over which the carbon concentration changes is much smaller than the distance over which it is effectively constant. Thus, the average concentration  $\bar{C}_C^{\gamma}$  is essentially equivalent to the concentration of carbon at sufficiently large distances from the grain boundary, at which the gradients of concentrations become effectively zero.

The mass balance for carbon requires that:

$$\Delta n_C^{\beta} = \Delta n_C^{\gamma} \quad (15)$$

Substituting eqs. (13) and (14) into eq. (15) and utilizing the expression for  $\bar{r}$  given by eq. (12), we obtain an expression for the carbon mole fraction in the grain:

$$\overline{x_C^\gamma} = x_C^0 - \frac{2\sqrt{D_{Cr}t}}{d\sqrt{\pi}} \frac{x_C^\beta - x_C^0}{x_{Cr}^\beta - x_{Cr}^0} (x_{Cr}^0 - x_{Cr}^{\gamma\beta}) \quad (16)$$

Eq. (16) is not an explicit expression for  $\overline{x_C^\gamma}$  because the interfacial chromium concentration  $x_{Cr}^{\gamma\beta}$  on the right-hand side of eq. (16) depends on the carbon concentration  $x_C^{\gamma\beta}$  through the paraequilibrium at the  $\gamma$ - $\beta$  interface. The paraequilibrium condition for the reaction of carbide formation (eq. 1) takes the form:

$$K = \frac{1}{(a_{Cr}^{\gamma\beta})^{\nu_{Cr}} (a_C^{\gamma\beta})^{\nu_C}} \quad (17)$$

where  $K$  is the equilibrium constant and the activities of Cr and C at the interface are denoted by  $a_{Cr}^{\gamma\beta}$  and  $a_C^{\gamma\beta}$ , respectively. In eq. (17), the activity of the carbide is equal to 1 because the carbide forms a separate phase. Eq. (17) can be written in a more convenient form by relating the equilibrium constant  $K$  to the Gibbs energy of formation  $\Delta G_f$ , i.e.,

$$\Delta G_f^0 = -RT \ln K \quad (18)$$

which can be expressed as a function of temperature as

$$\Delta G_f^0 = A + BT \quad (19)$$

Eq. (19) embodies the reasonable assumption that the enthalpy and entropy of formation are independent of temperature and is used to represent experimental Gibbs energy of formation data.<sup>33</sup> Rearrangement of eqs. (17) and (18) gives an expression for the activity of Cr at the grain boundary:

$$\ln a_{Cr}^{\gamma\beta} = \frac{1}{\nu_{Cr}} \left( \frac{\Delta G_f^0}{RT} - \nu_C \ln a_C^{\gamma\beta} \right) \quad (20)$$

Eq. (20) can be further rewritten by decomposing the activity into mole fractions and activity coefficients, i.e.,

$$\ln x_{Cr}^{\gamma\beta} \gamma_{Cr}^{\gamma\beta}(\mathbf{x}^{\gamma\beta}, T) = \frac{1}{\nu_{Cr}} \left( \frac{\Delta G_f^0}{RT} - \nu_C \ln x_C^{\gamma\beta} \gamma_C^{\gamma\beta}(\mathbf{x}^{\gamma\beta}, T) \right) \quad (21)$$

where the activity coefficients are functions of the vector of composition  $\mathbf{x}$  and temperature  $T$ . In addition to the thermodynamic equilibrium condition (21), the equality of carbon activities at the grain boundary and outside of the depletion zone (i.e.,  $a_C^{\gamma\beta} = a_C^\gamma$ ) provides another condition:

$$x_C^{\gamma\beta} \gamma_C^{\gamma\beta}(\mathbf{x}^{\gamma\beta}, T) = \overline{x_C^\gamma \gamma_C^\gamma}(\mathbf{x}^\gamma, T) \quad (22)$$

To apply eqs. (21) and (22), it is necessary to calculate the activity coefficients in the Cr-Ni-Fe-C system as a function of  $\mathbf{x}$  and  $T$ . For this purpose, we use the activity coefficient formulation developed by Babu<sup>34</sup> for Fe-Ni-Cr-Mo-C-N alloys on the basis of the models of Hertzman,<sup>35,36</sup> Hertzman and Jarl<sup>37</sup> and Andersson and Lange.<sup>38</sup> Conditions (21) and (22) are supplemented by the normalization condition for mole fractions:

$$\sum_i x_i^{\gamma\beta} = 1 \quad (23)$$

and the requirement that the molar ratio of the alloy components that do not participate in grain formation be constant in the grain.<sup>10</sup>

$$\frac{x_{Fe}^{\gamma\beta}}{x_{Ni}^{\gamma\beta}} = \frac{x_{Fe}^0}{x_{Ni}^0} \quad (24)$$

Equations (16) and (21-24) constitute a set of five equations, which can be solved numerically with respect to the four mole fractions at the interface,  $x_i^{\gamma\beta}$  ( $i = \text{Cr, Ni, Fe, C}$ ), and the mole fraction of carbon in the matrix outside of the depletion zone,  $\overline{x_C^\gamma}$ . The remaining mole fractions in the matrix outside of the depletion zone (i.e.,  $x_i^\gamma$  for  $i = \text{Cr, Ni, Fe}$ ) are essentially the same as those in the original alloy ( $x_i^0$ ) except for a slight renormalization to accommodate the changes in the matrix carbon concentration,  $\overline{x_C^\gamma}$ , in each iteration. In a practical implementation, the two linear constraints (eqs. 23 and 24) are used to eliminate two variables,  $x_{Fe}^{\gamma\beta}$  and  $x_{Ni}^{\gamma\beta}$ , which leaves three nonlinear equations (eqs. 16, 21, and 22) to be solved numerically. For optimum numerical stability, Eqs. (21) and (22) are then solved with respect to  $x_{Cr}^{\gamma\beta}$  and  $x_C^{\gamma\beta}$  for a given value of  $\overline{x_C^\gamma}$  in an inner loop and eq. (16) is converged with respect to  $\overline{x_C^\gamma}$  in an outer loop.

Once the value of  $x_{Cr}^{\gamma\beta}$  is found for a given temperature and time of exposure, the Cr concentration profile  $x_{Cr}^\gamma(z, t)$  is calculated from eq. (5) as a function of the distance  $z$  from the grain boundary and time. The corresponding concentration profiles of the other elements are then found from equations that are analogous to eqs. (23-24), but in which the local concentrations in the matrix,  $x_i^\gamma(z, t)$  ( $i = \text{Ni, Fe}$ ), are substituted instead of the grain boundary concentrations,  $x_i^{\gamma\beta}$ .

It should be noted that the thermodynamic model of carbide formation implies that the minimum chromium concentration is achieved at the very beginning of the heat exposure ( $t = 0$ ) because carbon concentration is then at its highest value. It is known, however, that the time to reach the minimum Cr concentration is finite rather than zero. Various approaches to account for this

observation have been proposed in the literature.<sup>13,29-31</sup> Here, we adopt the approach of Sourmail et al.,<sup>30</sup> who explained the delay in reaching the minimum of Cr depletion by considering the average composition that is measured rather than the exact predicted interface composition. Sourmail et al.<sup>30</sup> argued that the measurements are likely to overestimate the actual interface composition because of strong concentration gradients in the vicinity of the grain boundary, which cause the measured values to reflect an averaged effect due to beam spreading. Because of this effect, coupled with the problems of relative orientation of the grain boundary and the beam, Sourmail et al.<sup>30</sup> proposed to calculate the measurable concentration as the average over a finite range in a direction perpendicular to the boundary. At distances  $z$  close to the boundary, such an averaged value is significantly different from the local value when the concentration gradient is steep. As we move farther from the boundary, the average value rapidly approaches the local value. Thus, the averaged, measurable concentration at a distance  $z$  from the grain boundary is calculated as:

$$\overline{x_i^\gamma(z)} = \frac{1}{\Delta z} \int_{z-\Delta z/2}^{z+\Delta z/2} x(z) dz \quad (25)$$

where  $\Delta z$  is assumed to be 20 nm. The averaged value can be then compared with the results of experimental measurements. At distances close to the grain boundary, the averaged concentration naturally decreases as a function of time in a relatively short initial time interval, then reaches a minimum and finally increases.

This approach to calculating the measurable local concentration is sufficient for the study of localized corrosion because we are not concerned here with the detailed calculation of time evolution in the initial stages of chromium depletion. The accurate prediction of depletion profiles over a larger interval of time is much more important.

As discussed above, the growth of the carbide strongly depends on the volume (i.e.,  $V = Sd$ ) from which carbon is withdrawn. If the available distance  $d$  is small, the carbon concentration rapidly drops to the solubility limit and self-healing starts after a short amount of time. Conversely, if  $d$  is infinite, self-healing will never occur because the carbon concentration will remain at its bulk value. Following Sourmail et al.,<sup>30</sup> we assume that  $d$  is equal to one sixth of the average size of the grain because, in a simplified cubic model, six faces draw carbon from a given volume, i.e.,

$$d = \frac{g}{6} \quad (26)$$

where  $g$  is the average grain size.

In total, the chromium depletion model contains the following parameters:

- (a) Parameters  $A$  and  $B$  for calculating the Gibbs energy of formation of the carbide as a function of temperature (eq. 19)

(b) Parameters  $D_{Cr}^0$  and  $Q_{Cr}$  for calculating the diffusion coefficient of Cr as a function of temperature according to the general relation:

$$D_i = D_i^0 \exp \frac{Q_i}{RT} \quad (i = Cr) \quad (27)$$

(c) The average grain size  $g$ .

In principle, all these parameters can be obtained from independent experimental data, but they may be adjusted in practice to match concentration profile data.

#### *Extension of the model to Mo depletion*

Assuming that multicomponent diffusion effects can be neglected, the molybdenum concentration profile can be calculated from equations analogous to eqs. (2-5). The mole fraction of Mo as a function of time and distance from the grain boundary is then given by:

$$x_{Mo}^\gamma(z, t) = x_{Mo}^{\gamma\beta} + (x_{Mo}^0 - x_{Mo}^{\gamma\beta}) \operatorname{erf} \left( \frac{z}{2\sqrt{D_{Mo}t}} \right) \quad (28)$$

The accumulation of Mo in the carbide phase can be obtained from an equation analogous to eq. (6):

$$\Delta n_{Mo}^\beta = (C_{Mo}^\beta - C_{Mo}^0) S \bar{r} \quad (29)$$

As with Cr, the total depletion of Mo in the grain can be calculated by integrating the local depletion over the entire grain by using equations analogous to eqs. (7-10). This yields:

$$\Delta n_{Mo}^\gamma = \frac{S(x_{Mo}^0 - x_{Mo}^{\gamma\beta}) 2\sqrt{D_{Mo}t}}{V_m^\gamma \sqrt{\pi}} \quad (30)$$

Using the mass balance constraint for Mo, i.e.,

$$\Delta n_{Mo}^\beta = \Delta n_{Mo}^\gamma \quad (31)$$

an equation for the average dimension of the carbide along the z axis can be obtained:

$$\bar{r} = \frac{V_m^\beta (x_{Mo}^0 - x_{Mo}^{\gamma\beta}) 2\sqrt{D_{Mo}t}}{V_m^\gamma (x_{Mo}^\beta - x_{Mo}^0) \sqrt{\pi}} \quad (32)$$

Since the quantity  $\bar{r}$  obtained from eq. (32) must be the same as that obtained from eq. (12), we obtain a relationship between the mole fractions of Mo and Cr at the  $\gamma$ - $\beta$  boundary:

$$x_{Mo}^{\gamma\beta} = x_{Mo}^0 - (x_{Cr}^0 - x_{Cr}^{\gamma\beta}) \frac{x_{Mo}^{\beta} - x_{Mo}^0}{x_{Cr}^{\beta} - x_{Cr}^0} \sqrt{\frac{D_{Cr}}{D_{Mo}}} \quad (33)$$

To apply eq. (33), it is necessary to know the mole fractions in the carbide phase,  $x_{Mo}^{\beta}$  and  $x_{Cr}^{\beta}$ . For this purpose, we assume the overall metal carbide stoichiometry  $M_{\nu_M} C_{\nu_C}$ , where the typical values of  $\nu_M$  and  $\nu_C$  are 23 and 6 or 7 and 3, respectively. Then, we can write:

$$\frac{x_{Cr}^{\beta} + x_{Mo}^{\beta}}{x_C^{\beta}} = \frac{\nu_M}{\nu_C} \quad (34)$$

In addition, it is necessary to specify the ratio of the mole fractions of Mo and Cr in the carbide phase, i.e.,

$$\frac{x_{Mo}^{\beta}}{x_{Cr}^{\beta}} = m \quad (35)$$

In principle, this value can be obtained from experimental measurements. In some cases (e.g., in alloy 825,<sup>14</sup> this ratio does not differ much, on average, from the molar ratio of Mo to Cr in the bulk alloy. In the absence of experimental data, the ratio  $m$  can be assumed to be equal to that in the bulk alloy as a default value. From eqs. (34) and (35), the mole fractions in the carbide phase can be calculated as

$$x_{Mo}^{\beta} = \frac{m \frac{\nu_M}{\nu_C}}{(1+m) \left( 1 + \frac{\nu_M}{\nu_C} \right)} \quad (36)$$

$$x_{Cr}^{\beta} = \frac{\frac{\nu_M}{\nu_C}}{(1+m) \left( 1 + \frac{\nu_M}{\nu_C} \right)} \quad (37)$$

In the next step, it is necessary to generalize the thermodynamic paraequilibrium relationships for carbide formation (eqs. 1 and 17-21). Reaction (1) can be generalized for a mixed carbide:



The formation reaction (eq. 38) can be formally separated using two thermodynamically equivalent forms:

$$\frac{v_{Cr}}{v_M}(v_M Cr + v_C C) + \frac{v_{Mo}}{v_M}(v_M Mo + v_C C) = Cr_{v_{Cr}} Mo_{v_{Mo}} C_{v_C} \quad (39)$$

and

$$\frac{v_{Cr}}{v_M} Cr_{v_M} C_{v_C} + \frac{v_{Mo}}{v_M} Mo_{v_M} C_{v_C} = Cr_{v_{Cr}} Mo_{v_{Mo}} C_{v_C} \quad (40)$$

Hence, it is convenient to decompose eq. (38) into two reactions:

$$v_M Cr + v_C C = Cr_{v_M} C_{v_C} \quad (41)$$

$$v_M Mo + v_C C = Cr_{v_M} C_{v_C} \quad (42)$$

Following eqs. (17-20), it is easy to show that the thermodynamic relations for eqs. (41) and (42) are

$$\ln a_{Cr}^{\gamma\beta} = \frac{1}{v_M} \left( \frac{\Delta G_f^0(Cr_{v_M} C_{v_C})}{RT} - v_C \ln a_C^{\gamma\beta} \right) \quad (43)$$

$$\ln a_{Mo}^{\gamma\beta} = \frac{1}{v_M} \left( \frac{\Delta G_f^0(Mo_{v_M} C_{v_C})}{RT} - v_C \ln a_C^{\gamma\beta} \right) \quad (44)$$

The main advantage of this decomposition is the fact that eq. (43) is algebraically equivalent to eqs. (20) or (21). Eqs. (16) and (22-24) remain unchanged for systems containing Mo. Thus, the system is described by seven equations, i.e., (43), (44), (16), (22-24), and (33), which can be solved with respect to the five mole fractions at the interface,  $x_i^{\gamma\beta}$  ( $i = Cr, Mo, Ni, Fe, C$ ), and the mole fraction of carbon in the matrix outside of the depletion zone,  $\overline{x_C^\gamma}$ . Since one of the equations is redundant, it is convenient to use eq. (33) and eliminate eq. (44) because eq. (33) provides a straightforward linear constraint and the additional thermodynamic parameter  $\Delta G_f^0(Mo_{v_M} C_{v_C})$  does not need to be then known. After solving eqs. (43), (16), (22-24), and (33), eq. (44) may be used for testing the consistency of the solution as long as  $\Delta G_f^0(Mo_{v_M} C_{v_C})$  can be evaluated with sufficient accuracy.

Using this approach, calculation of depletion profiles for molybdenum-containing systems requires two additional parameters in addition to those used for computing the Cr depletion profiles as described above, i.e.,

- (d) The diffusion coefficient of Mo, which is calculated from the standard equation (27) where  $i = Mo$  and
- (e) The Mo/Cr molar ratio in the carbide (eq. 35), which can be obtained from experimental data or adjusted based on Mo depletion profiles.

### *Effective size of depletion zone*

To evaluate the width of the depletion zone in a direction perpendicular to the grain boundary, it is convenient to define the effective size of the depletion zone. The depletion profile does not automatically define the size of the depletion zone because it asymptotically approaches the bulk concentration of Cr (cf. Fig. 1, upper diagram). Therefore, to evaluate the effective size of the depletion zone  $z_{eff}$ , we can approximate the chromium depletion zone by a triangle with the vertices defined by  $C_{Cr}^0$  and  $C_{Cr}^{\gamma\beta}$  along the concentration axis (cf. Fig. 1) and  $z_{eff}$  along the  $z$  axis. Then, the total depletion of chromium,  $\Delta n_{Cr}^\gamma$ , calculated from the triangular approximation should be equal to that obtained by rigorous integration from zero to infinity (eq. 10). From simple geometrical considerations, the total depletion calculated using the approximate triangle is equal to:

$$\Delta n_{Cr}^\gamma = S \left( C_{Cr}^0 - C_{Cr}^{\gamma\beta} \right) \frac{z_{eff}}{2} = \frac{1}{2} \frac{S}{V_m^\beta} \left( x_{Cr}^0 - x_{Cr}^{\gamma\beta} \right) z_{eff} \quad (45)$$

By equating  $\Delta n_{Cr}^\gamma$  calculated from eqs. (10) and (45), we obtain

$$z_{eff} = \frac{4\sqrt{D_{Cr}t}}{\sqrt{\pi}} \quad (46)$$

### ***Repassivation potential model***

In a previous paper,<sup>19</sup> a comprehensive model was developed for calculating the repassivation potential of base alloys as a function of environment chemistry and temperature. The model was derived by considering the dissolution of a metal in a localized corrosion environment in the limit of repassivation. The model envisages the dissolution of the metal (M) underneath a layer of a concentrated metal halide solution MX. In the process of repassivation, a thin layer of oxide is assumed to form at the interface between the metal and the hydrous metal halide. The model represents the formation of the oxide layer using a partial coverage approach. The partial coverage fraction increases as repassivation is approached. The dissolution rate of the metal under the oxide is lower than at the metal-halide interface and corresponds to the passive dissolution rate. Thus, as the repassivation potential is approached, the dissolution rate tends towards the passive dissolution rate. The model includes the effects of multiple aggressive and non-aggressive or inhibitive species, which are assumed to undergo competitive adsorption. The aggressive species form metal complexes, which dissolve in the active state. The inhibitive species and water contribute to the formation of oxides, which induce passivity. The formalism that describes these phenomena leads to a closed-form equation in the limit of repassivation, i.e., when the current density reaches a predetermined low value  $i_{rp}$  (assumed to be  $i_{rp} = 10^{-2}$  A/m<sup>2</sup>) and the fluxes of metal ions become small and comparable to those for passive dissolution. Most importantly for the study of the repassivation potential of heat-treated alloys, the parameters of the model have been generalized in terms of alloy composition for Fe-Ni-Cr-Mo-W-N alloys.<sup>24</sup>

This generalization was based on experimental  $E_{rp}$  data for thirteen base (typically mill-annealed) stainless steels and nickel-base alloys, supplemented by those for Fe and Ni. The Appendix summarizes the final working equations for the  $E_{rp}$  model, defines the model parameters and provides the equations for calculating the parameters as functions of alloy composition. Thus, the Appendix contains a complete recipe for predicting the repassivation potential as a function of alloy composition, aqueous environment temperature, and chloride activity. This model will be used further in this study to predict the repassivation potentials of heat-treated alloys.

### *Effective repassivation potential of sensitized alloys*

Unlike the degree of sensitization, the repassivation potential of sensitized samples is not merely a reflection of Cr depletion below a certain threshold level.<sup>18</sup> In contrast to intergranular dissolution, which occurs primarily in the Cr-depleted regions, pitting/crevice corrosion can occur in both Cr-depleted and non-depleted areas. Further, the rate of dissolution inside a pit or active crevice region is not likely to be dramatically different between a Cr-depleted and non-depleted material because localized corrosion occurs in a completely active state in a highly aggressive environment. In repassivation potential tests, the potential at which the rate of oxide film formation exceeds the active dissolution rate is measured as a function of heat treatment. This process is expected to be different between the Cr-depleted and non-depleted areas, leading to a different potential at which the oxide film is stabilized as a function of local alloy composition.

The repassivation potential model described above can be directly used to predict local values of  $E_{rp}$  on the basis of the local Cr (and Mo) concentration as a function of the distance from the grain boundary. However, such local values of  $E_{rp}$  are not experimentally accessible. This is due to the fact that the measured repassivation potential is a macroscopic property, i.e., it reflects the repassivation of several pits with dimensions ranging from several hundred micrometers to a millimeter. These dimensions are much larger than the depletion zone sizes and, therefore, each pit can be imagined to contain several depleted grain boundaries at the bottom of the pit. In principle, it would be possible to calculate the averaged repassivation potential if the geometry of the pit was exactly known and the composition of the alloy that is exposed to the pit environment could be exactly ascertained. However, such information is not available in practice and, even if it were available, prediction of  $E_{rp}$  based on detailed measurements of individual pits would be of little predictive value for corroding structures. Instead, it is necessary to establish a procedure for estimating the average repassivation potential for statistically distributed pits. For this purpose, it is reasonable to make the following assumptions:

- (a) The measured  $E_{rp}$  primarily reflects the localized corrosion of the Cr-depleted regions rather than the surfaces whose Cr concentration is given by the nominal alloy composition. This is due to the fact that a pit stabilizes more easily in an area that is more susceptible to localized corrosion due to chromium (or molybdenum) depletion. Thus, the average repassivation potential should be calculated by integrating the  $E_{rp}$  over the depleted zone.
- (b) A pit needs to achieve a certain minimum size to be stabilized in an  $E_{rp}$  measurement. Therefore, in the case of a narrow Cr depletion zones, the averaging should extend beyond the depletion zone to ensure that a certain minimum area of the alloy contributes to the measurable  $E_{rp}$ .

Following assumption (a), the average repassivation potential,  $\overline{E_{rp}}$ , can be obtained by integration of the local repassivation potential,  $E_{rp}(z)$ , as follows:

$$\overline{E_{rp}} = \frac{\int_0^L w(z) E_{rp}(z) dz}{\int_0^L w(z) dz} \quad (47)$$

where  $L$  is the distance from the grain boundary over which the integration is performed and  $w(z)$  is a weighting factor, which reflects, in principle, the uneven contribution of the depleted zone surface to the observable repassivation potential. In view of assumption (a) the distance for integration,  $L$ , can be identified with the effective size of the depletion zone,  $z_{eff}$  (eq. 46).

However, this value should be adjusted in agreement with assumption (b) to ensure that the repassivation potential is integrated over at least a certain reasonable minimum distance from the grain boundary. Thus, the distance for integration can be estimated as

$$L = z_{eff} + 2\Delta z \quad (48)$$

where  $z_{eff}$  is calculated from eq. (46) and  $2\Delta z$  is the minimum size for stabilization of localized corrosion. For simplicity,  $\Delta z$  is set at the same value as that used to calculate the observable depletion profiles (eq. 25). The expression for  $z_{eff}$  obtained from eq. (46) is somewhat arbitrary because a different value could be obtained, for example, on the basis of the molybdenum depletion profile. However, the precise definition of the effective size is not crucial for integrating the repassivation potential over the depletion zone. With eq. (48), the repassivation potential is effectively integrated over the depletion zone when the zone is reasonably wide. When it is very narrow, the integration is effectively performed over the minimum distance.

The weighting factor  $w(z)$  for the integration should recognize that the contribution of the depleted areas with Cr concentration below the threshold value (e.g.,  $x_{Cr}^* = 0.12$ ) should be greater than the contribution of the areas in which Cr is less severely depleted. For this purpose, we define  $w(z)$  as follows:

$$w(z) = 1 + \eta \max\left(\frac{x_{Cr}^* - x_{Cr}(z)}{x_{Cr}^*}, 0\right) \quad (49)$$

In eq. (49), the term in parentheses ensures that weighting factor is equal to 1 for all chromium concentrations above the threshold value (i.e., when  $x_{Cr}(z) \geq x_{Cr}^*$ ) and becomes progressively enhanced as the Cr concentration drops below  $x_{Cr}^*$ . The enhancement factor  $\eta$  is assumed to be equal to 100, which is the order of magnitude of the elevation of dissolution rates in Cr-depleted

areas in standard tests in acidic solutions. While eq. (49) is arbitrary, it provides a reasonable enhancement of the weighting factor for the Cr compositions that fall below  $x_{Cr}^*$ . The minimum value of  $w(z)$  is 1 while the maximum value is  $1+\eta$ .

Thus, the averaged repassivation potential for heat-treated samples can be obtained from eqs. (47-49), where the local value of the repassivation potential  $E_{rp}(z)$  is calculated from the generalized repassivation potential model (as described in the Appendix) using the local alloy compositions obtained from the calculated Cr and Mo depletion profiles as a function of the distance from the grain boundary.

## Results and Discussion

In this section, we first verify the grain boundary microchemistry model by comparing the calculated depletion profiles with experimental data. Then, we calculate the repassivation potential of thermally aged and welded alloys.

The grain boundary microchemistry model has been verified using experimental data for alloys 600, 825, and 316L. The parameters  $A$  and  $B$  were determined by regressing depletion data simultaneously for various samples of a given alloy. The only sample-specific parameter is the average grain size and the remaining parameters are general for a given alloy. However, the predicted depletion profiles are much less sensitive to the grain size than to the remaining parameters and the effect of grain size manifests itself only at relatively advanced stages of healing because the grain size determines the available supply of carbon.

In the case of alloy 600, experimental data are available from three sources.<sup>8,10,39</sup> These three data sets are in reasonably good agreement with each other. Model calculations are compared with selected experimental data in Figure 2. The two diagrams in Figure 2 illustrate the progressive self-healing (i.e., the increase in the minimum Cr concentration and the concomitant widening of the depletion profiles) for sensitized samples aged at 973 K (Fig. 2a) and 923 K (Fig. 2b) as a function of aging time. For comparison, depletion profiles are also shown for lower aging temperature and longer aging time (873 K, 250 h) and higher temperature and shorter time (1073 K, 0.42 h). Good agreement has been obtained with all data sets, in particular with the data of Was and Kruger.<sup>10</sup>

For alloy 825, chromium depletion data are available from the study of Pan et al.<sup>14</sup> Figure 3 compares the calculated and experimental results for this alloy. The time evolution of the depletion profiles is shown for samples thermally aged at 913 K (Fig. 3a) and at temperatures ranging from 973 to 1073 K (Fig. 3b). Because of a higher Cr content of alloy 825 compared with that of alloy 600, the grain boundary Cr concentration does not drop to values as low as those observed in Figure 2. The model calculations are in agreement with the data within the experimental scattering range. To calculate both Cr and Mo depletion profiles, it was assumed that the Mo/Cr ratio in the carbide is identical to that in the bulk alloy, which is consistent with the carbide composition results reported by Pan et al.<sup>14</sup> However, molybdenum depletion profiles are not available for this alloy so that a comparison cannot be made.

On the other hand, some experimental Mo depletion profiles are available for type 316L stainless steel. Selected results of calculations are shown for this alloy in Figure 4. Figure 4a shows the time evolution of depletion profiles for a relatively low aging temperature (823 K) and long times. Figure 4b illustrates the Cr depletion profiles for a fixed aging time (1000 h) and temperatures varying from 873 K to 1023 K. The widening of the profiles and the increase in the minimum Cr concentration as a function of aging temperature at constant aging time are correctly reproduced. Figure 4c shows the molybdenum depletion profile at the conditions that correspond to the Cr profiles in Figure 4a. For type 316L stainless steel, the Mo/Cr ratio was adjusted to reproduce the depletion profiles. Thus, the model simultaneously reproduces the Cr and Mo depletion profiles generally within the uncertainty of experimental data.

After verifying the predicted depletion profiles, the methodology described above has been applied to predicting the repassivation potential. Figures 5 and 6 show the results of modeling the repassivation potential for alloy 600. Figure 5 summarizes the dependence of the repassivation potential of mill-annealed samples on temperature and the activity of chloride ions.<sup>24</sup> The lines in Figure 5 have been obtained from the correlation described in the Appendix. Over most of the chloride range,  $E_{rp}$  shows the standard semi-logarithmic dependence on chloride activity. This dependence provides a baseline for calculating  $E_{rp}$  of thermally aged samples.

Figure 6 shows the difference between the repassivation potentials of solution annealed and thermally aged samples and those of mill-annealed samples, i.e.,

$$\Delta E_{rp} = E_{rp} - E_{rp, \text{mill-annealed}} \quad (50)$$

The experimental  $E_{rp}$  data have been reported in a previous paper<sup>18</sup> for samples aged at 700 °C as a function of time. The repassivation potentials have been measured at 60 °C in 0.001M, 0.005M, and 0.04M NaCl solutions. The measurements have been performed on alloy 600 with 0.02% C at all conditions and on the alloy with 0.04% C in 0.001M and 0.04M NaCl solutions. In Figure 6, the thick lines show the averaged repassivation potentials predicted according to equations (48-50). The thin lines represent the minimum value of the repassivation potential, which corresponds to the minimum predicted concentration of chromium at the grain boundary. The experimental data are plotted with error bars of  $\pm 50$  mV, which is a reasonable estimate of the uncertainty of  $E_{rp}$  measurements. Comparison between the calculated and experimental values reveals that the model predictions agree, in general, with the data for the 0.02C alloy within the experimental scattering range. Although the scattering of the data is substantial, both the data and the calculated curves show the same trends. For the 0.04C alloy, the agreement is poorer in 0.001M solutions since the experimental data indicate an increase in  $E_{rp}$  over the values for mill-annealed samples whereas the model predictions do not show a healing effect.

The repassivation potential initially drops fairly rapidly as a function of aging time and then slowly recovers towards the  $E_{rp}$  value of the annealed sample (which is indicated by the horizontal line in Fig. 6). This behavior parallels the evolution of chromium depletion as a function of aging time. Although the calculated  $E_{rp}$  values can never exceed the repassivation potential of the bulk alloy, some of the experimental data lie above the horizontal line for  $\Delta E_{rp}=0$ . This apparently unphysical behavior may be due to an incomplete homogenization of the annealed samples, which may later proceed to completion as a result of the self-healing process.

If the experimental points that lie above the  $\Delta E_{rp}=0$  line are neglected, the calculated lines are in reasonably good agreement with experimental data.

The depression of  $E_{rp}$  as a function of aging time is slightly deeper for the 0.04% C alloy compared with the 0.02% alloy, which reflects a lower concentration of chromium in the depleted zone of the alloy with a higher carbon content. This is illustrated in Figure 7, which compares the predicted depletion profiles after 2.5h and 96h of thermal aging for the 0.02% C and 0.04% C lots. Further, the higher carbon content has a substantial effect on the predicted recovery of the repassivation potential as a function of aging time, i.e., the recovery is notably slower for the alloy with a higher carbon content.

Results of calculations for alloy 825 are summarized in Figures 8 and 9. In contrast to alloy 600, alloy 825 contains an appreciable amount of molybdenum. Therefore, the predicted repassivation potential depends on the molybdenum profile in addition to the chromium profile. To calculate molybdenum depletion, it has been assumed that the molar Mo/Cr ratio in the carbide (eq. 35) is the same as in the bulk alloy. This is consistent with measurements of grain boundary carbide compositions reported by Pan et al.<sup>14</sup>

The baseline results for the repassivation potential of mill-annealed alloy 825 are shown in Figure 8 as a function of chloride ion activity and temperature.<sup>19,40</sup> The plot of  $E_{rp}$  versus chloride activity exhibits a change in slope, which is characteristic of many corrosion resistant alloys and is consistent with the repassivation potential model.<sup>19</sup> While the slope is low and similar to that observed for alloy 600 at higher chloride concentrations, it becomes more steep in dilute solutions. As in Figure 5, the lines have been obtained from the generalized correlation described in the Appendix.

The  $E_{rp}$  measurements for thermally aged samples were performed at 95 °C in 100 ppm (0.00282 M)  $Cl^-$  solutions. These conditions are close to the transition between the high-slope and low-slope segments of the  $E_{rp}$  vs.  $Cl^-$  activity plot, at which the repassivation potential is sensitive to environmental conditions. The calculated and experimental depression in the repassivation potential ( $\Delta E_{rp}$ ) is shown in Figure 9 for samples aged for 15 h and 100 h as a function of aging temperature. In contrast to alloy 600, the predicted minimum values of  $E_{rp}$  (thin lines) are much lower than the averaged values (thick lines). The predicted averaged values are in excellent agreement with experimental data for samples aged for 15 h (circles in Fig. 9). For the samples aged for 100 h, the agreement is good for lower aging temperatures but the  $E_{rp}$  depression is underestimated for higher temperatures. However, the predicted  $\Delta E_{rp}$  is consistent with the observed self-healing at higher temperatures after 100 h, which is indicated by the depletion profiles. Therefore, these deviations may be due to the incomplete self-healing of the samples used in the  $E_{rp}$  measurements.

It should be noted that the  $E_{rp}$  depression of austenitic alloys (both calculated and experimental) is relatively modest. Much larger depressions are observed for duplex alloys.<sup>41</sup> However, the mechanism of chromium depletion in duplex alloys is different. The calculation of the repassivation potential of heat treated duplex alloys will be the subject of a forthcoming paper. Also, the model will be applied to predict the localized corrosion behavior of welded samples.

## Conclusions

A general procedure has been developed for predicting the effect of thermal aging on the repassivation potential of austenitic alloys. The procedure combines two mechanistic models – a grain boundary microchemistry model for calculating the chromium and molybdenum depletion profiles in the vicinity of grain boundaries and an electrochemical model that relates the repassivation potential to alloy composition as well as temperature and solution chemistry. The grain boundary microchemistry model accurately reproduces the experimental Cr and Mo depletion profiles for sensitized alloys 600, 825, and 316L. Since the microchemistry model utilizes only well-defined physical parameters, it is applicable to alloys with different composition. Using the previously developed  $E_{rp}$  model, a methodology has been established to calculate the observable repassivation potential by integrating the  $E_{rp}$  values that correspond to the local alloy chemistry in the depletion zone. Such averaged values are in satisfactory agreement with experimental  $E_{rp}$  data that have been measured in chloride solutions for thermally aged samples of alloy 600 and 825.

## Acknowledgements

The work reported here has been supported by the U.S. Department of Energy (award number DE-FC36-04GO14043) and co-sponsored by ChevronTexaco, DuPont, Haynes International, Mitsubishi Chemical, Shell, and Toyo Engineering.

## Appendix: Generalized Correlation for Predicting the Repassivation Potential

In a general case of a system containing  $NA$  aggressive ions and  $NI$  inhibitive ions, the repassivation potential  $E_{rp}$  is obtained by solving an equation given by:

$$1 + \sum_k^{NI} \left[ \left( \frac{i_{rp}}{i_p} - 1 \right) \frac{l_k''}{i_{rp}} \right] \theta_k^{n_k} \exp\left( \frac{\xi_k F E_{rp}}{RT} \right) = \sum_j^{NA} \frac{k_j''}{i_{rp}} \theta_j^{n_j} \exp\left( \frac{\alpha_j F E_{rp}}{RT} \right) \quad (\text{A-1})$$

where  $i_p$  is the passive current density,  $i_{rp}$  is the current density threshold that defines repassivation ( $i_{rp} = 10^{-2}$  A/m<sup>2</sup>),  $\theta_j$  is the partial surface coverage fraction by solution species  $j$ ,  $T$  is the temperature,  $R$  is the gas constant,  $F$  is the Faraday constant and  $k_j''$ ,  $l_k''$ ,  $n_j$ ,  $n_k$ ,  $\alpha_j$ , and  $\xi_k$  are electrochemical kinetic parameters as defined below. The summation on the right-hand side of eq. (A-1) is performed over all aggressive species ( $j = 1, \dots, NA$ ) and the summation on the left-hand side pertains to inhibitive species ( $k = 1, \dots, NI$ ). The H<sub>2</sub>O molecules are treated as inhibitive species because they contribute to the formation of the oxide layer. The electrochemical parameters of the model are defined as follows:

- (i) The quantity  $k_j''$  is the reaction rate constant for alloy dissolution mediated by the adsorption of aggressive species  $j$ . This constant is used in a scaled form (i.e., as  $k_j = k_j'' / i_{rp}$ ) and is expressed using a scaled Gibbs energy of activation  $\Delta g_{A,j}^\ddagger$ :

$$k_j = \frac{k_j''}{i_{rp}} = \exp\left(-\frac{\Delta g_{A,j}^\ddagger}{RT}\right) \quad (\text{A-2})$$

- (ii) The quantity  $l_k''$  is the reaction rate constant for the formation of oxide mediated by the adsorption of inhibitive species  $k$ . It is also used in a scaled form, i.e., as  $l_k = \left(\frac{i_{rp}}{i_p} - 1\right) \frac{l_k''}{i_{rp}}$  and is expressed using a scaled Gibbs energy of activation  $\Delta g_{I,k}^\ddagger$ :

$$l_k = \left(\frac{i_{rp}}{i_p} - 1\right) \frac{l_k''}{i_{rp}} = \exp\left(-\frac{\Delta g_{I,k}^\ddagger}{RT}\right) \quad (\text{A-3})$$

- (iii) The quantities  $n_j$  and  $n_k$  are the reaction rate orders with respect to the aggressive species  $j$  and inhibitive species  $k$ , respectively.  
(iv) The parameters  $\alpha_j$  and  $\xi_k$  are the electrochemical transfer coefficients for the reactions involving the aggressive species  $j$  and inhibitive species  $k$ , respectively. The parameter  $\alpha_j$  has been assumed to be equal to one for simplicity.

The partial coverage fraction of a species  $j$  is related to the activity of this species in the bulk solution through an adsorption isotherm, i.e.,

$$\theta_j = \frac{r_j a_j}{1 + \sum_k r_k a_k} \quad (\text{A-4})$$

where the adsorption coefficient is defined using the Gibbs energy of adsorption  $\Delta G_{ads,i}$ , i.e.,

$$r_j = \exp\left(-\frac{\Delta G_{ads,j}}{RT}\right) \quad (\text{A-5})$$

For  $\text{H}_2\text{O}$  in aqueous solutions,  $\theta_{\text{H}_2\text{O}}$  is assumed to be equal to one for simplicity. For calculating the temperature dependence of the kinetic parameters, the scaled Gibbs energies of activation are further related to temperature as

$$\frac{\Delta g_{A,j}^\ddagger}{T} = \frac{\Delta g_{A,j}^\ddagger(T_{ref})}{T_{ref}} + \Delta h_{A,j}^\ddagger \left(\frac{1}{T} - \frac{1}{T_{ref}}\right) \quad (\text{A-6})$$

for aggressive ions and

$$\frac{\Delta g_{I,k}^\ddagger}{T} = \frac{\Delta g_{I,k}^\ddagger(T_{ref})}{T_{ref}} + \Delta h_{I,k}^\ddagger \left(\frac{1}{T} - \frac{1}{T_{ref}}\right) \quad (\text{A-7})$$

for water and inhibitive species. In eqs. (A-6) and (A-7), the parameters  $\Delta g_{A,j}^{\ddagger}(T_{ref})$  and  $\Delta g_{I,k}^{\ddagger}(T_{ref})$  are the scaled Gibbs energies of activation at reference temperature  $T_{ref} = 298.15$  K for the reactions mediated by the adsorption of aggressive and inhibitive ions, respectively. The quantities  $\Delta h_{A,j}^{\ddagger}$  and  $\Delta h_{I,k}^{\ddagger}$  are the corresponding enthalpies of activation.

The environments considered in this study are limited to one kind of aggressive species (i.e., the  $Cl^-$  ions) and one kind of inhibitive species (i.e., the  $H_2O$  molecules). In such a case, the repassivation potential is characterized, in the most general case, by seven parameters, i.e.,  $\Delta g_{A,Cl}^{\ddagger}(T_{ref})$ ,  $\Delta h_{A,Cl}^{\ddagger}$ ,  $n_{A,Cl}$ ,  $\Delta g_{I,H_2O}^{\ddagger}(T_{ref})$ ,  $\Delta h_{I,H_2O}^{\ddagger}$ ,  $\xi_{I,H_2O}$ , and  $\Delta G_{ads,Cl}$ . In a previous study,<sup>24</sup> generalized expressions for these parameters have been developed. Specifically, the Gibbs energy of adsorption of ions ( $\Delta G_{ads,Cl}$ ), the electrochemical transfer coefficient for the formation of passive oxide as a result of a reaction with water ( $\xi_{I,H_2O}$ ) and the reaction order with respect to  $Cl^-$  ions ( $n_{A,Cl}$ ) have been set equal to common values, i.e.,

$$\Delta G_{ads,Cl} / (kJ / mol) = 10 \quad (A-8)$$

$$\xi_{I,H_2O} = 0.8 \quad (A-9)$$

$$n_{A,Cl} = 1.1 \quad (A-10)$$

The enthalpies of activation  $\Delta h_{A,Cl}^{\ddagger}$  and  $\Delta h_{I,H_2O}^{\ddagger}$  have been found to be linearly related to the respective Gibbs energies of activation  $\Delta g_{A,Cl}^{\ddagger}(T_{ref})$  and  $\Delta g_{I,H_2O}^{\ddagger}(T_{ref})$ , i.e.,

$$\Delta h_{A,Cl}^{\ddagger} = 0.055 + 0.002\Delta g_{A,Cl}^{\ddagger}(T_{ref}) \quad (A-11)$$

$$\Delta h_{I,H_2O}^{\ddagger} = -0.015 + 0.032\Delta g_{I,H_2O}^{\ddagger}(T_{ref}) \quad (A-12)$$

Finally, the two Gibbs energies of activation  $\Delta g_{A,Cl}^{\ddagger}(T_{ref})$  and  $\Delta g_{I,H_2O}^{\ddagger}(T_{ref})$  have been expressed in terms of alloy composition for Fe-Ni-Cr-Mo-W-N alloys. The Gibbs energy of activation for dissolution mediated by adsorption of aggressive species ( $\Delta g_{A,Cl}^{\ddagger}(T_{ref})$ ) is calculated as a sum of four contributions, i.e.,

$$\Delta g_{A,Cl}^{\ddagger}(T_{ref}) = \Delta g_{A,Cl}^{\ddagger}(Cr, Fe, Ni) + \Delta g_{A,Cl}^{\ddagger}(Mo, W) + \Delta g_{A,Cl}^{\ddagger}(N) + \Delta g_{A,Cl}^{\ddagger}(misc) \quad (A-13)$$

where  $\Delta g_{A,Cl}^{\ddagger}(Cr, Fe, Ni)$  is the baseline contribution for Fe-Ni-Cr alloys,  $\Delta g_{A,Cl}^{\ddagger}(Mo, W)$  is an increment due to the effect of Mo and W,  $\Delta g_{A,Cl}^{\ddagger}(N)$  is an increment due to N and

$\Delta g_{A,Cl}^{\ddagger}(misc)$  is a miscellaneous contribution of other elements. The baseline contribution for Fe-Ni-Cr alloys is given by:

$$\Delta g_{A,Cl}^{\ddagger}(Cr, Fe, Ni) = \Delta g_{A,Cl}^{\ddagger}(Fe)w_{Fe} + \Delta g_{A,Cl}^{\ddagger}(Ni)w_{Ni} + 398.5w_{Cr}w_{Ni}^{0.7} + 555.9w_{Cr}w_{Fe}^{0.7} - 335.4w_{Cr} \quad (A-14)$$

where  $\Delta g_{A,Cl}^{\ddagger}(Fe) = -74.1$  and  $\Delta g_{A,Cl}^{\ddagger}(Ni) = -18.7$  are the Gibbs energies of activation for iron (or, for practical purposes, carbon steel) and nickel, respectively. The remaining contributions are calculated as

$$\Delta g_{A,Cl}^{\ddagger}(Mo,W) = w_{Cr}(w_{Mo} + w_W)^{0.4}(893.9w_{Ni}^{1.7} + 839.0w_{Fe}^{1.7}) \quad (A-15)$$

$$\Delta g_{A,Cl}^{\ddagger}(N) = w_N^{0.5}w_{Cr}^3[-1.293e5w_{Fe}^{0.2} + 1.451e5w_{Ni}^{0.2}] \quad (A-16)$$

$$\Delta g_{A,Cl}^{\ddagger}(misc) = -1764w_{Nb}w_{Cr} \quad (A-17)$$

With the current database, the  $\Delta g_{A,Cl}^{\ddagger}(misc)$  term is limited to the effect of Nb and should be treated as tentative. An expression similar to eq. (A-13) has been adopted for the Gibbs energy of activation for the formation of oxide mediated by adsorption of H<sub>2</sub>O, i.e.,

$$\Delta g_{I,H_2O}^{\ddagger}(T_{ref}) = \Delta g_{I,H_2O}^{\ddagger}(Cr,Fe,Ni) + \Delta g_{I,H_2O}^{\ddagger}(Mo,W) + \Delta g_{I,H_2O}^{\ddagger}(N) + \Delta g_{I,H_2O}^{\ddagger}(misc) \quad (A-18)$$

where

$$\Delta g_{I,H_2O}^{\ddagger}(Cr,Fe,Ni) = 18.14w_{Fe} + 169.6w_{Ni} + 1983w_{Cr}^{1.1} \quad (A-19)$$

$$\Delta g_{I,H_2O}^{\ddagger}(Mo,W) = -2422\left[(w_{Mo} + w_W)^{1.1} + w_{Cr}^{1.1}(w_{Fe} + 1.4w_{Ni})\right] + 2024\left[(w_{Mo} + w_W)^{1.1}(w_{Fe}^{0.5} + w_{Ni}^{0.5})\right] \quad (A-20)$$

$$\Delta g_{I,H_2O}^{\ddagger}(N) = w_N^{0.5}w_{Cr}^3[-2.607d5w_{Fe}^{0.2} + 2.384e5w_{Ni}^{0.2}] \quad (A-21)$$

$$\Delta g_{I,H_2O}^{\ddagger}(misc) = -4950w_{Nb}w_{Cr} \quad (A-22)$$

Eqs. (A-1) through (A-22) constitute a generalized correlation for predicting  $E_{rp}$  of Fe-Ni-Cr-Mo-W-N alloys as a function of composition. The overall average deviation between the calculated results and experimental data for all alloys is 67 mV.<sup>24</sup> The effect of ions other than Cl<sup>-</sup> can be also included as discussed in a previous study,<sup>24</sup> but such ions are outside of the scope of this work.

## References

1. A.J. Sedriks, Corrosion of Stainless Steels, J. Wiley & Sons, New York, 1996.
2. S. Lamb (ed.): CASTI Handbook of Stainless Steels and Nickel-Base Alloys, CASTI Publishing, Edmonton, Canada, 2001.
3. J.R. Davis (ed.) Corrosion of Weldments, ASM International, Materials Park, OH, 2006.
4. C. Stawström and M. Hillert: J. Iron Steel Inst. 1969, January, 77-85.
5. C.S. Tedmon Jr., D.A. Vermilyea and J.H. Rosolowski: J. Electrochem. Soc. 1969, 118, 192-202.

6. V. Cihal: Intergranular Corrosion of Steels and Alloys, Mater. Sci. Monographs, vol. 18, Elsevier, New York, NY, 1984.
7. E.L. Hall and C.L. Briant: Metallurg. Trans. A. 1984, 15A, 793-811
8. E.L. Hall and C.L. Briant: Metall. Trans. A, 1985, 16A, 1225-1236.
9. S.M. Bruemmer and L.A. Charlot: Scripta Metall. 1986, 20, 1019-1024.
10. G.S. Was and G.M. Kruger: Acta Metallurgica, 1985, 33, 841-854.
11. G.S. Was: Corrosion, 1990, 46, 319-330.
12. J.J. Kai, G.P. Yu, C.H. Tsai, M.N. Liu and S.C. Yao: Metall. Trans. A, 1989, 20A, 2057-2067.
13. W.E. Mayo: Mater. Sci. Eng., 1997, A232: 129-139.
14. Y.-M. Pan, D.S. Dunn, G.A. Cragolino and N. Sridhar: Metall. Mater. Trans. A, 2000, 31A, 1163-1173.
15. D.S. Dunn, D. Daruwalla and Y.-M. Pan, "Effect of Fabrication Processes on Material Stability – Characterization and Corrosion", Report CNWRA 2004-01, Southwest Research Institute, 2004.
16. D.S. Dunn, Y.-M. Pan, L. Yang and G.A. Cragolino: Corrosion, 2006, 62, 3-12.
17. D.S. Dunn, O. Pensado, Y.-M. Pan, R.T. Pabalan, L. Yang, X. He, and K.T. Chiang, "Passive and Localized Corrosion of Alloy 22 - Modeling and Experiments", Report CNWRA 2005-02, Southwest Research Institute, 2005.
18. G. Tormoen, N. Sridhar and A. Anderko, "Localised Corrosion of Heat-Treated Alloys. I. Repassivation Potential of Alloy 600 as a Function of Solution Chemistry and Thermal Aging", submitted to Corr. Eng. Sci. Technol, 2008.
19. A. Anderko, N. Sridhar and D.S. Dunn: Corrosion Sci., 2004, 46, 1583-1612.
20. N. Sridhar, C.S. Brossia, D.S. Dunn and A. Anderko: Corrosion, 2004, 60, 915-936.
21. D.S. Dunn, N. Sridhar, and G.A. Cragolino: Corrosion, 1996, 52, 115-124.
22. D.S. Dunn, G.A. Cragolino and N. Sridhar, Corrosion, 2000, 56, 90-104.
23. A. Anderko, N. Sridhar, L.T. Yang, S.L. Grise, B.J. Saldanha and M.H. Dorsey, Corros. Eng. Sci. Technol. 2005, 40, 33-42.
24. A. Anderko, N. Sridhar, M.A. Jakab and G. Tormoen, A General Model for the Repassivation Potential as a Function of Multiple Aqueous Species. 2. Effect of Oxyanions on Localized Corrosion of Fe-Ni-Cr-Mo-W-N Alloys, submitted for publication.
25. R.L. Fullman: Acta Metall. 1982, 30, 1407-1415.
26. R.M. Kruger, G.S. Was, J.F. Mansfield and J.R. Martin: Acta Metall. 1988, 36, 3163-3176.
27. B.W. Bennett and H.W. Pickering: Acta Metall., 1988, 36, 539-546.
28. S.M. Bruemmer: Corrosion, 1990, 46, 698-709.
29. H. Sahlaoui, H. Sidhom and J. Philibert: Acta Materialia, 2002, 50: 1383-1392.

30. T. Sourmail, C.H. Too and H.K.D.H. Bhadeshia: ISIJ International, 2003, 43, 1814-1820.
31. Y.F. Yin and R.G. Faulkner: Corrosion Sci. 2007, 49, 2177-2197.
32. J. Crank, The Mathematics of Diffusion, 2<sup>nd</sup> Ed., Clarendon Press, Oxford, 1975.
33. F.D. Richardson, J. Iron Steel. Inst. 1953, 175, 33-51.
34. S.S. Babu, in A. Anderko, P. Wang, R. D. Young, D. P. Riemer, P. McKenzie, M. M. Lencka, S. S. Babu, P. Angelini, “Prediction of Corrosion of Alloys in Mixed-Solvent Environments”, Final report for the project DE-FC07-00CH11019, DOE Office of Industrial Technologies, June 2003, [www.osti.gov/servlets/purl/811533-wUOQwz/native/](http://www.osti.gov/servlets/purl/811533-wUOQwz/native/), subtask 1.1.
35. S. Hertzman, Metal. Trans. A, 1987, 18A, 1753-1766.
36. S. Hertzman, Metal. Trans. A. 1987, 18A, 1767-1778.
37. S. Hertzman and M. Jarl, Metall. Trans. A, 1987, 18A, 1745-1752.
38. J.-O. Andersson and N. Lange, Metal. Trans. 1988, 19A, 1385-1394.
39. G.S. Was, H.H. Tischner and R.M. Latanision: Metall. Trans. A, 1981, 12A, 1397-1408
40. N. Sridhar and G.A. Cragolino: Corrosion, 1993, 49, 885-894.
41. T. Amadou, A. Ben Rhouma, H. Sidhom, C. Braham and J. Ledion, Metall. Mater. Trans. A, 2000, 31A, 2015-2024.
42. H. Sahlaoui, K. Makhlof, H. Sidhom and J. Philibert: Mat. Sci. Eng. A, 2004, 372, 98-108.
43. A. Tekin, J.W. Martin and B.A. Senior, J. Materials Sci. 1991, 26, 2458-2466.

**Table 1. Nominal compositions of the alloys studied**

Alloy	UNS No.	Nominal composition, weight percent					
		Ni	Fe	Cr	Mo	C	Other
600	N06600	bal.	8.0	15.5	0	0.02 (lot 1) 0.04 (lot 2)	
825	N08825	bal.	33.5	21.5	3.0	0.01	Cu = 2
316L	S31603	10.0	bal.	17.0	2.5	0.03, max	
C-22*	N06022	bal.	3.0	22.0	13.0	0.01	W = 3

\* - Registered Trademark of Haynes International

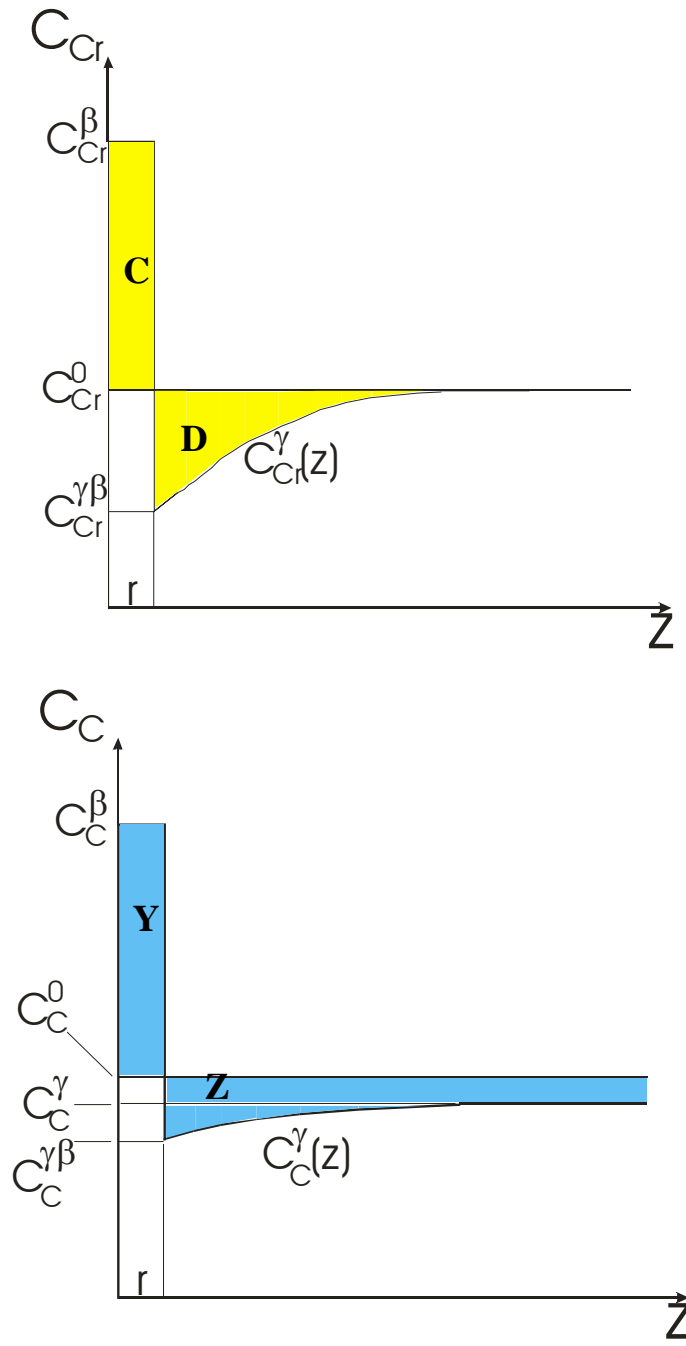
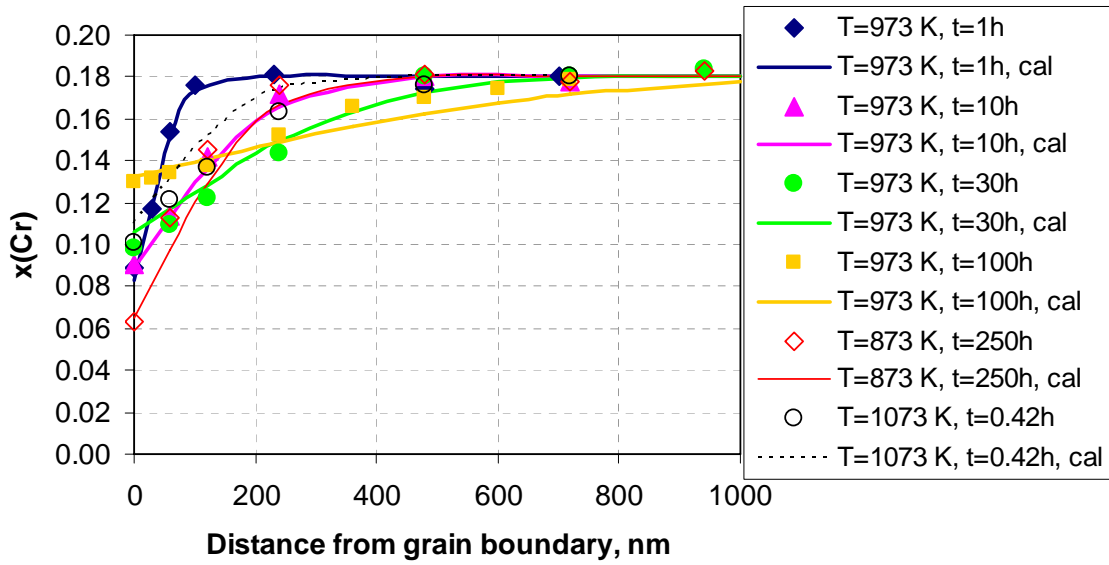


Figure 1. Scheme of grain boundary material balance calculations for Cr (upper diagram) and C (lower diagram). The concentrations of Cr and C and denoted by  $C_{Cr}$  and  $C_C$ , respectively. The superscripts 0,  $\beta$ ,  $\gamma$ , and  $\gamma\beta$  denote the concentrations in the original alloy, the carbide phase, the bulk alloy, and at the alloy-carbide boundary, respectively. The distance from the grain boundary is denoted by  $z$  and the  $r$  is the the dimension of the grain boundary precipitate.

a.



b.

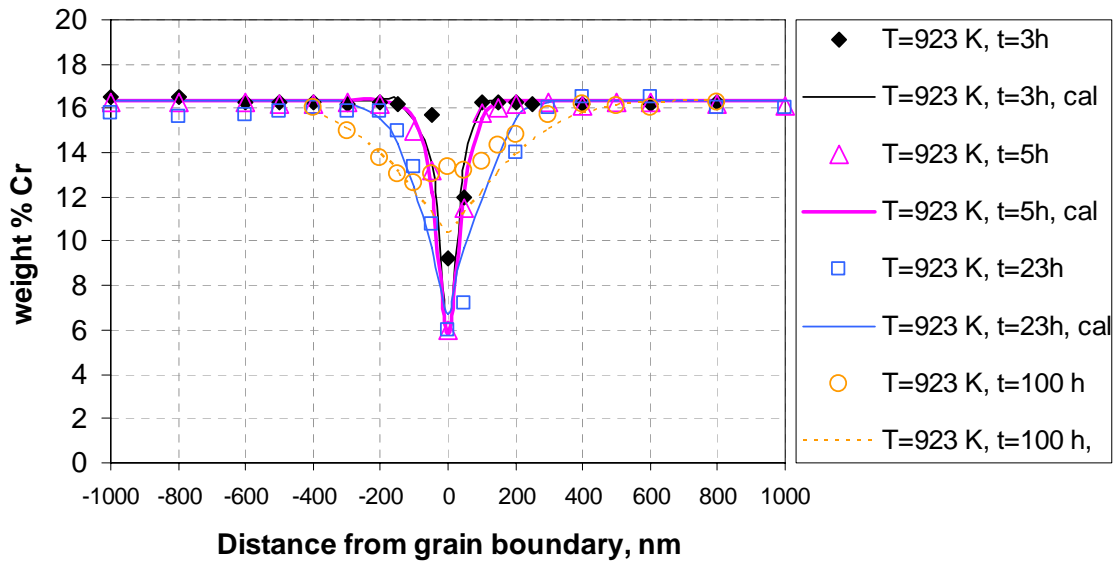
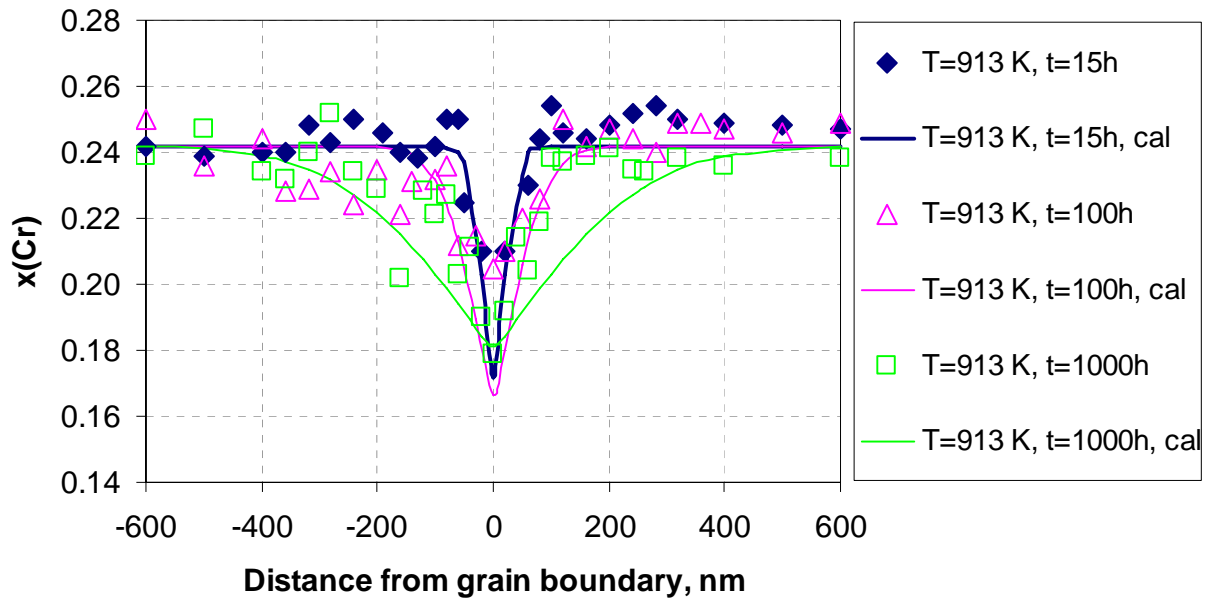


Figure 2. Calculated and experimental chromium depletion profiles of heat-treated alloy 600 for various aging temperatures and times. The experimental data are from Was and Kruger<sup>10</sup> (diagram a) and Hall and Briant<sup>8</sup> (diagram b).

a.



b.

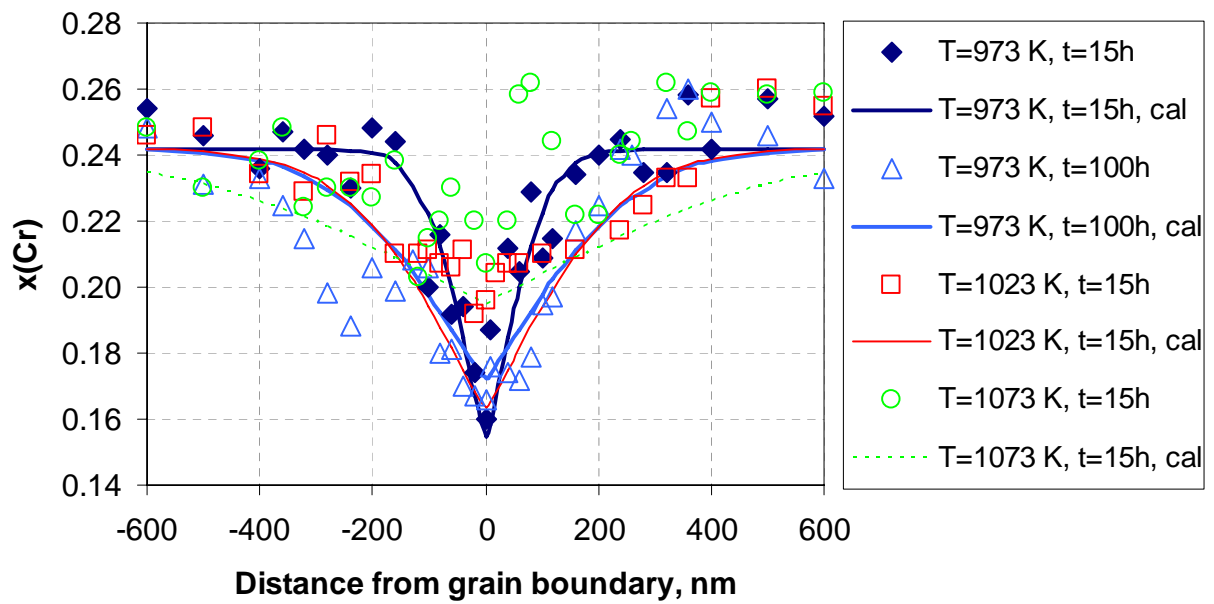


Figure 3. Calculated and experimental chromium depletion profiles for alloy 825 thermally aged at 913 K (diagram a) and 973-1073 K (diagram b). The experimental data are from Pan et al.<sup>14</sup>

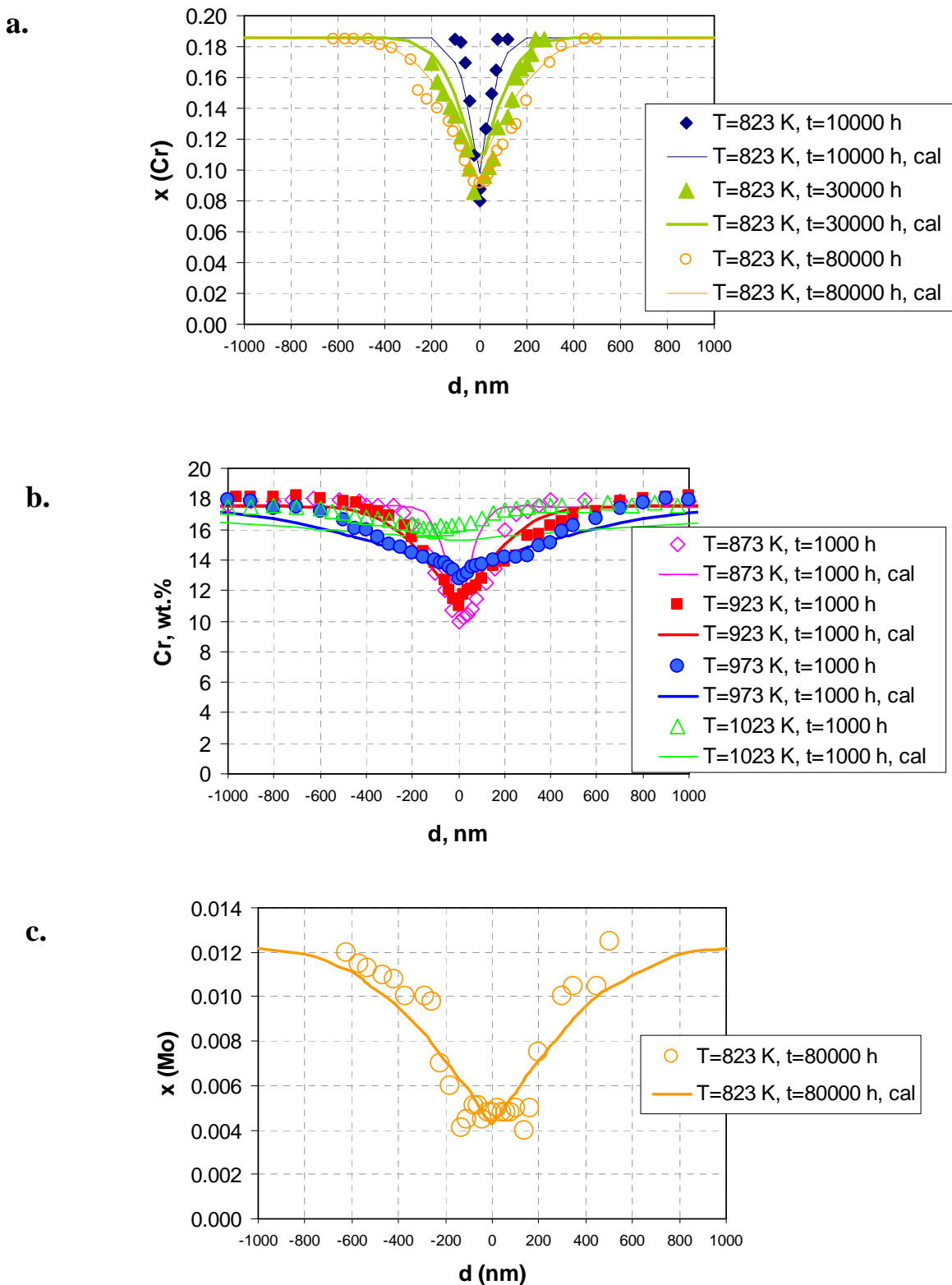


Figure 4. Calculated and experimental chromium (diagrams a, b) and molybdenum (diagram c) depletion profiles for heat-treated type 316 stainless steel. The data are from Sahlaoui et al.<sup>42</sup> (diagrams a, c) and Tekin et al.<sup>43</sup> (diagram b).

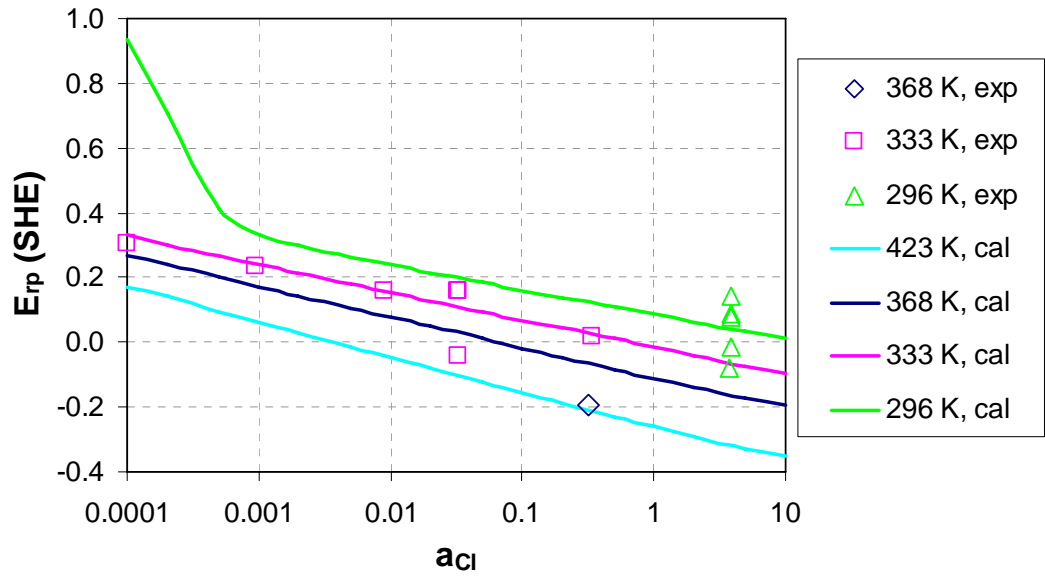


Figure 5. Effect of chloride activity and temperature on the repassivation potential of mill-annealed alloy 600.

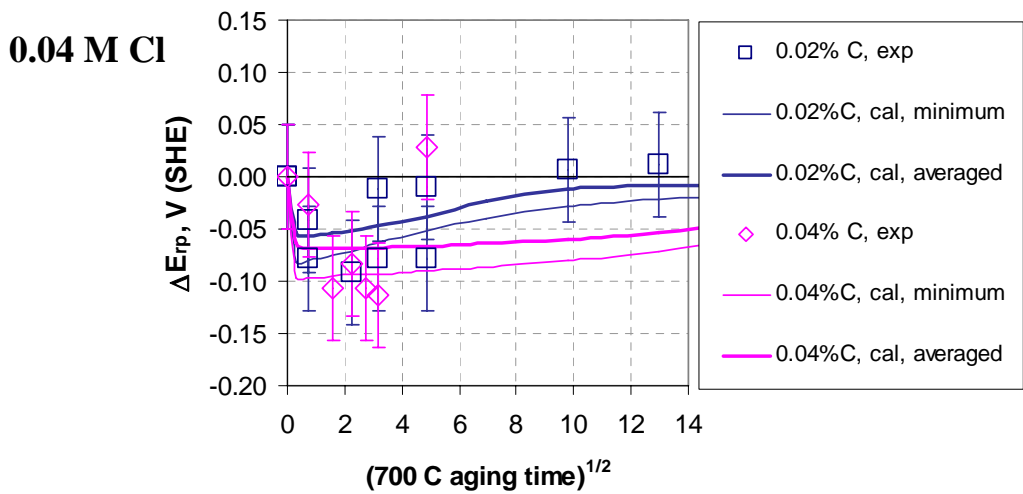
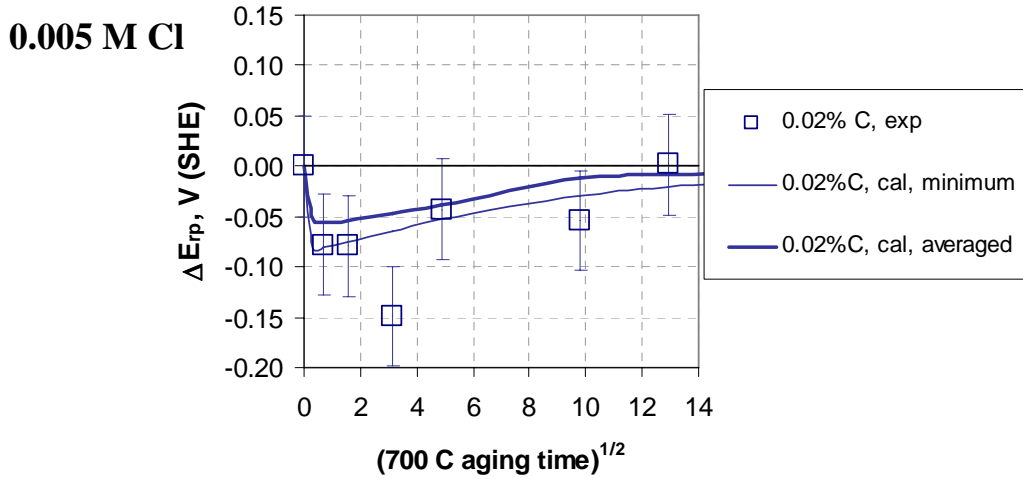
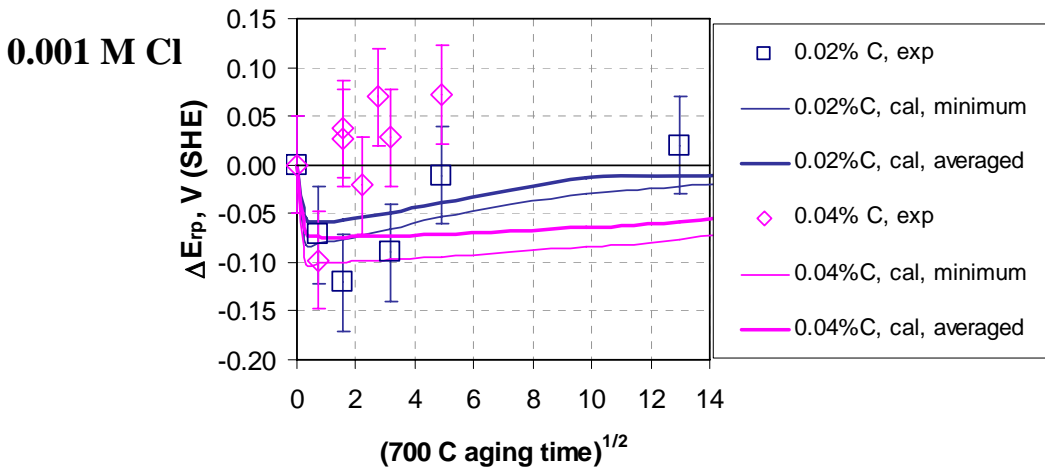


Figure 6. Predicted and experimental depression of the repassivation potential ( $\Delta E_{rp} = E_{rp} - E_{rp,annealed}$ ) of alloy 600 heat-treated at 700 °C. The repassivation potential was obtained at 60 °C in 0.001M, 0.005M, and 0.04M NaCl solutions.

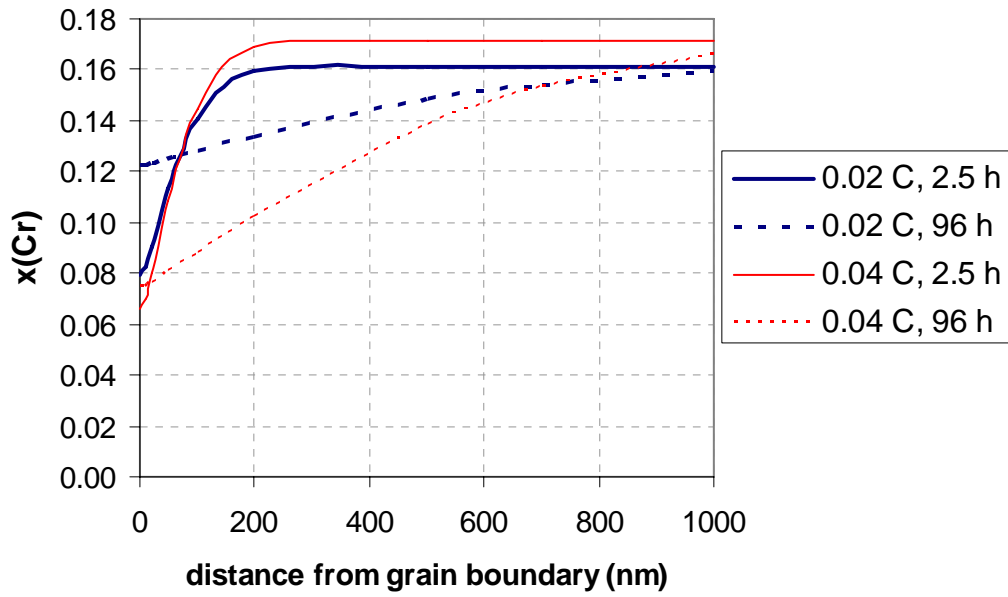


Figure 7. Predicted Cr depletion profiles for the 0.02% C (lot 1) and 0.04% C (lot 2) samples used for  $E_{rp}$  measurements after heat treatment at 700 °C.

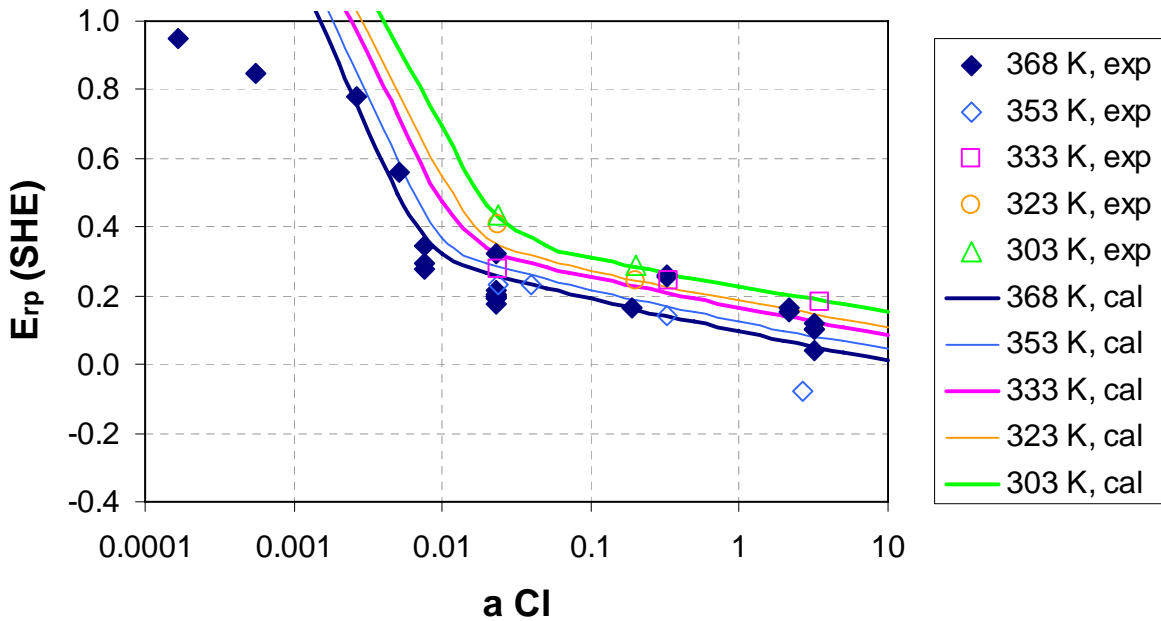


Figure 8. Effect of chloride activity and temperature on the repassivation potential of mill-annealed alloy 825. The experimental data are from Sridhar and Cragolino<sup>40</sup> and Anderko et al..<sup>19</sup>

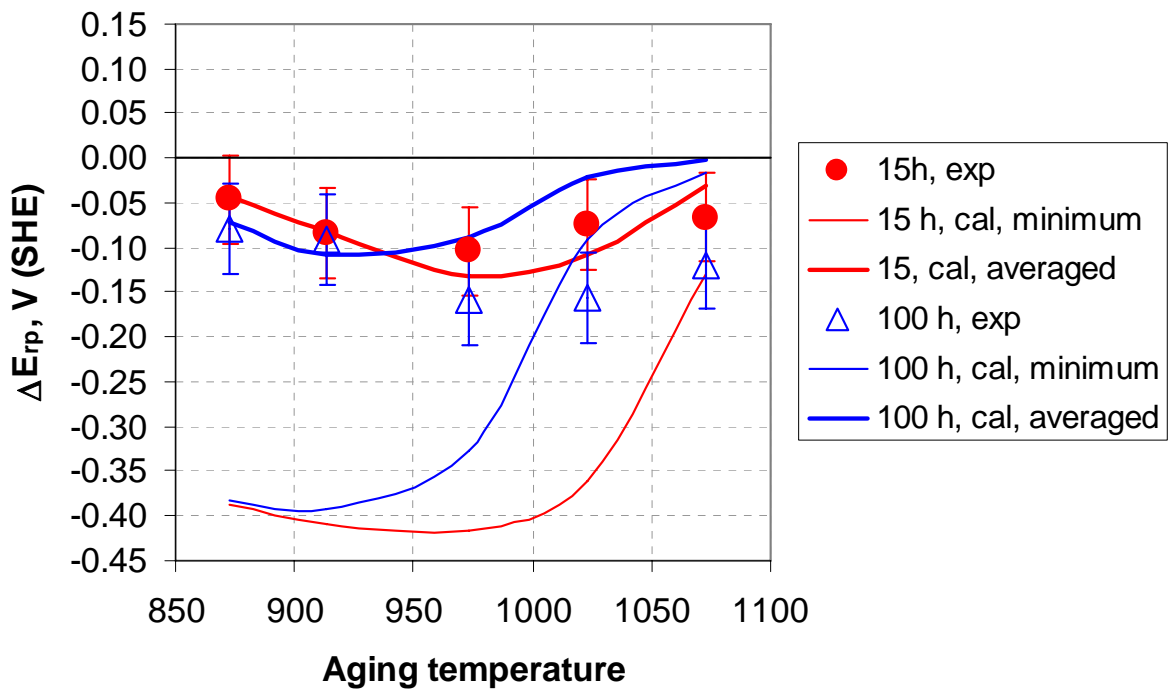


Figure 9. Predicted and experimental depression of the repassivation potential ( $\Delta E_{rp} = E_{rp} - E_{rp,annealed}$ ) of alloy 825 heat-treated at various temperatures. The repassivation potential was obtained at 95 °C in 100 ppm (0.00282 M)  $Cl^-$  solutions.<sup>14</sup>